

1 The gene expression landscape of the human locus coeruleus 2 revealed by single-nucleus and spatially-resolved transcriptomics

3 4 Authors

5 Lukas M. Weber^{1,*}, Heena R. Divecha^{2,*}, Matthew N. Tran², Sang Ho Kwon^{2,3}, Abby Spangler², Kelsey
6 D. Montgomery², Madhavi Tippani², Rahul Bharadwaj², Joel E. Kleinman^{2,4}, Stephanie C. Page²,
7 Thomas M. Hyde^{2,4,5}, Leonardo Collado-Torres², Kristen R. Maynard^{2,4}, Keri Martinowich^{2,3,4,6,*},
8 Stephanie C. Hicks^{1,*}

9 10 Affiliations

- 11 1 Department of Biostatistics, Johns Hopkins Bloomberg School of Public Health, Baltimore, MD, 21205, USA
- 12 2 Lieber Institute for Brain Development, Johns Hopkins Medical Campus, Baltimore, MD, 21205, USA
- 13 3 Department of Neuroscience, Johns Hopkins School of Medicine, Baltimore, MD, 21205, USA
- 14 4 Department of Psychiatry and Behavioral Sciences, Johns Hopkins School of Medicine, Baltimore, MD,
15 21205, USA
- 16 5 Department of Neurology, Johns Hopkins School of Medicine, Baltimore, MD, 21205, USA
- 17 6 The Kavli Neuroscience Discovery Institute, Johns Hopkins University, Baltimore, MD, 21205, USA

18 19 * equal contribution

20

21 Correspondence

22 Stephanie C. Hicks
23 shicks19@jhu.edu

24

25 Keri Martinowich
26 keri.martinowich@libd.org

27 Abstract

28 Norepinephrine (NE) neurons in the locus coeruleus (LC) project widely throughout the central nervous
29 system, playing critical roles in arousal and mood, as well as various components of cognition including
30 attention, learning, and memory. The LC-NE system is also implicated in multiple neurological and
31 neuropsychiatric disorders. Importantly, LC-NE neurons are highly sensitive to degeneration in both
32 Alzheimer's and Parkinson's disease. Despite the clinical importance of the brain region and the
33 prominent role of LC-NE neurons in a variety of brain and behavioral functions, a detailed molecular
34 characterization of the LC is lacking. Here, we used a combination of spatially-resolved transcriptomics
35 and single-nucleus RNA-sequencing to characterize the molecular landscape of the LC region and the
36 transcriptomic profile of LC-NE neurons in the human brain. We provide a freely accessible resource of
37 these data in web-accessible formats.

38

39 Keywords

40 Locus coeruleus, norepinephrine, spatially-resolved transcriptomics, single-nucleus RNA-sequencing,
41 postmortem human tissue

42 Introduction

43 The locus coeruleus (LC) is a small bilateral nucleus located in the dorsal pons of the brainstem, which
44 serves as the brain's primary site for production of the neuromodulator norepinephrine (NE). NE-
45 producing neurons in the LC project widely to many regions of the central nervous system to modulate
46 a variety of highly divergent functions including attention, arousal, and mood [1–4]. The LC, translated
47 as “blue spot”, comprises merely 3,000 NE neurons in the rodent (~1500-1600 each side of the
48 brainstem) [1], and estimates in the human LC range from 19,000-46,000 total NE neurons [5]. Despite
49 its prominent involvement in a number of critical brain functions and its unique capacity to synthesize
50 NE, the LC's small size and deep positioning within the brainstem has rendered it relatively intractable
51 to a comprehensive cellular, molecular, and physiological characterization.

52
53 The LC plays important roles in core behavioral and physiological brain function across the lifespan and
54 in disease. For example, there is strong evidence for age-related cell loss in the LC [6,7], and the LC-
55 NE system is implicated in multiple neuropsychiatric and neurological disorders [4,8]. The LC is one of
56 the earliest sites of degeneration in Alzheimer's disease (AD) and Parkinson's disease (PD), and
57 profound loss of LC-NE neurons is evident with disease progression [8–10]. Moreover, maintaining the
58 neural density of LC-NE neurons prevents cognitive decline during aging [11]. In addition, primary
59 neuropathologies for AD (hyperphosphorylated tau) and PD (alpha-synuclein) can be detected in the
60 LC prior to other brain regions [12–15]. However, the molecular mechanisms rendering LC-NE neurons
61 particularly vulnerable to age-related decline and neurodegeneration are not well-understood. In
62 addition to its role in aging, the LC-NE system plays a critical role in mediating sustained attention, and
63 its dysregulation is associated with attention-deficit hyperactivity disorder (ADHD) [16,17]. Of note, the
64 NE reuptake inhibitor atomoxetine is the first non-stimulant medication that is FDA-approved for ADHD
65 [18–20]. Better understanding the gene expression landscape of the LC and surrounding region and
66 delineating the molecular profile of LC-NE neurons in the human brain could facilitate the ability to
67 target these neurons for disease prevention or manipulate their function for treatment.

68
69 The recent development of single-nucleus RNA-sequencing (snRNA-seq) and spatially-resolved
70 transcriptomics (SRT) technological platforms provides an opportunity to investigate transcriptome-wide
71 gene expression scale with cellular and spatial resolution [21,22]. SRT has recently been used to
72 characterize transcriptome-wide gene expression within defined neuroanatomy of cortical regions in the
73 postmortem human brain [22], while snRNA-seq has been used to investigate specialized cell types in
74 a number of postmortem human brain regions including medium spiny neurons in the nucleus
75 accumbens and dopaminergic neurons in the midbrain [21,23]. Importantly, snRNA-seq and SRT
76 provide complementary views: snRNA-seq identifies transcriptome-wide gene expression within
77 individual nuclei, while SRT captures transcriptome-wide gene expression in all cellular compartments
78 (including the nucleus, cytoplasm, and cell processes) while retaining the spatial coordinates of these
79 measurements. While not all SRT platforms achieve single-cell resolution, depending on the
80 technological platform and tissue cell density, spatial gene expression has been resolved at, for
81 example, ~1-10 cells per spatial measurement location with a diameter of 55 μm in the human brain
82 [22]. These platforms have been successfully used in tandem to spatially map single-nucleus gene
83 expression in several regions of both neurotypical and pathological tissues in the human brain including
84 the dorsolateral prefrontal cortex [22] and the dopaminergic substantia nigra [21].

85

86 In this report, we characterize the gene expression signature of the LC and surrounding region at
87 spatial resolution, and identify and characterize a population of NE neurons at single-nucleus resolution
88 in the neurotypical adult human brain. In addition to NE neurons, we identify a population of 5-
89 hydroxytryptamine (5-HT, serotonin) neurons, which have not previously been characterized at the
90 molecular level in human brain samples [24]. We observe expression of cholinergic marker genes
91 within NE neurons, and confirm that this is due to co-expression within individual cells using fluorescent
92 labeling with high-resolution imaging. We compare our findings from the human LC and adjacent region
93 to molecular profiles of LC and peri-LC neurons that were previously characterized in rodents using
94 alternative technological platforms [25–27], and observe partial conservation of LC-associated genes
95 across these species.
96

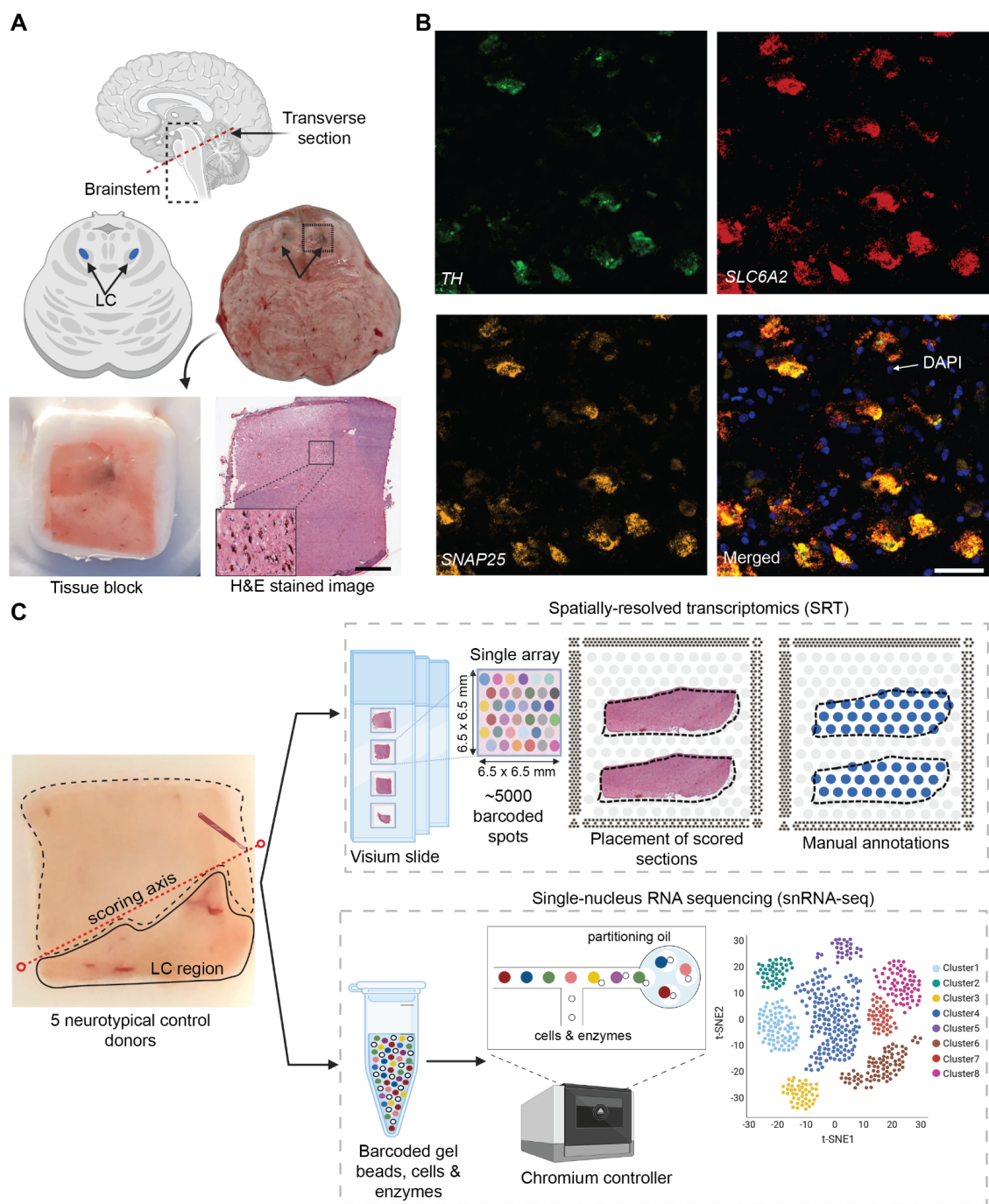
97 Results

98 Experimental design and study overview of postmortem human LC

99 We selected 5 neurotypical adult human brain donors to characterize transcriptome-wide gene
100 expression within the LC at spatial and single-nucleus resolution using the 10x Genomics Visium SRT
101 [28] and 10x Genomics Chromium snRNA-seq [29] platforms (see **Supplementary Table 1** for donor
102 demographic details). In each tissue sample, the LC was first visually identified by neuroanatomical
103 landmarks and presence of neurons containing the pigment neuromelanin on transverse slabs of the
104 pons (**Figure 1A**). Prior to SRT and snRNA-seq assays, we ensured that the tissue blocks
105 encompassed the LC by probing for known LC marker genes [30]. Specifically, we cut 10 μ m
106 cryosections from tissue blocks from each donor and probed for the presence of a pan-neuronal marker
107 gene (*SNAP25*) and two NE neuron-specific marker genes (*TH* and *SLC6A2*) by multiplexed single-
108 molecule fluorescence *in situ* hybridization (smFISH) using RNAscope [31,32] (**Figure 1B**). Robust
109 mRNA signal from these markers, visualized as puncta on imaged tissue sections, was used as a
110 quality control measure in all tissue blocks prior to proceeding with inclusion in the study and
111 performing SRT and snRNA-seq assays.
112

113 For tissue blocks included in the study, we cut additional 10 μ m tissue sections, which were used for
114 gene expression profiling at spatial resolution using the 10x Genomics Visium SRT platform [28]
115 (**Figure 1C**). Fresh-frozen tissue sections were placed onto each of four capture areas per Visium slide,
116 where each capture area contains approximately 5,000 expression spots (spatial measurement
117 locations with diameter 55 μ m and 100 μ m center-to-center, where transcripts are captured) laid out in
118 a honeycomb pattern. Spatial barcodes unique to each spot are incorporated during reverse
119 transcription, thus allowing the spatial coordinates of the gene expression measurements to be
120 identified [28]. Visium slides were stained with hematoxylin and eosin (H&E), followed by high-
121 resolution acquisition of histology images prior to on-slide cDNA synthesis, completion of the Visium
122 assay, and sequencing. For our study, 10 μ m tissue sections from the LC-containing tissue blocks were
123 collected from the 5 brain donors, with assays completed on 2-4 tissue sections per donor. Given the
124 small size of the LC compared to the area of the array, tissue blocks were scored to fit 2-3 tissue
125 sections from the same donor onto a single capture area to maximize the use of the Visium slides,
126 resulting in a total of $N=9$ Visium capture areas (hereafter referred to as samples).
127

128 For 3 of the 5 donors, we cut additional 100 μ m sections from the same tissue blocks to profile
129 transcriptome-wide gene expression at single-nucleus resolution with the 10x Genomics Chromium
130 single cell 3' gene expression platform [29] (**Figure 1C**). Prior to collecting tissue sections, the tissue
131 blocks were scored to enrich for NE neuron-containing regions. Neuronal enrichment was employed
132 with fluorescence-activated nuclear sorting (FANS) prior to library preparation to enhance capture of
133 neuronal population diversity, and snRNA-seq assays were subsequently completed. **Supplementary**
134 **Table 1** provides a summary of SRT and snRNA-seq sample information and demographic
135 characteristics of the donors.
136
137



138

139

140

141

142

143

144

145

146

147

148

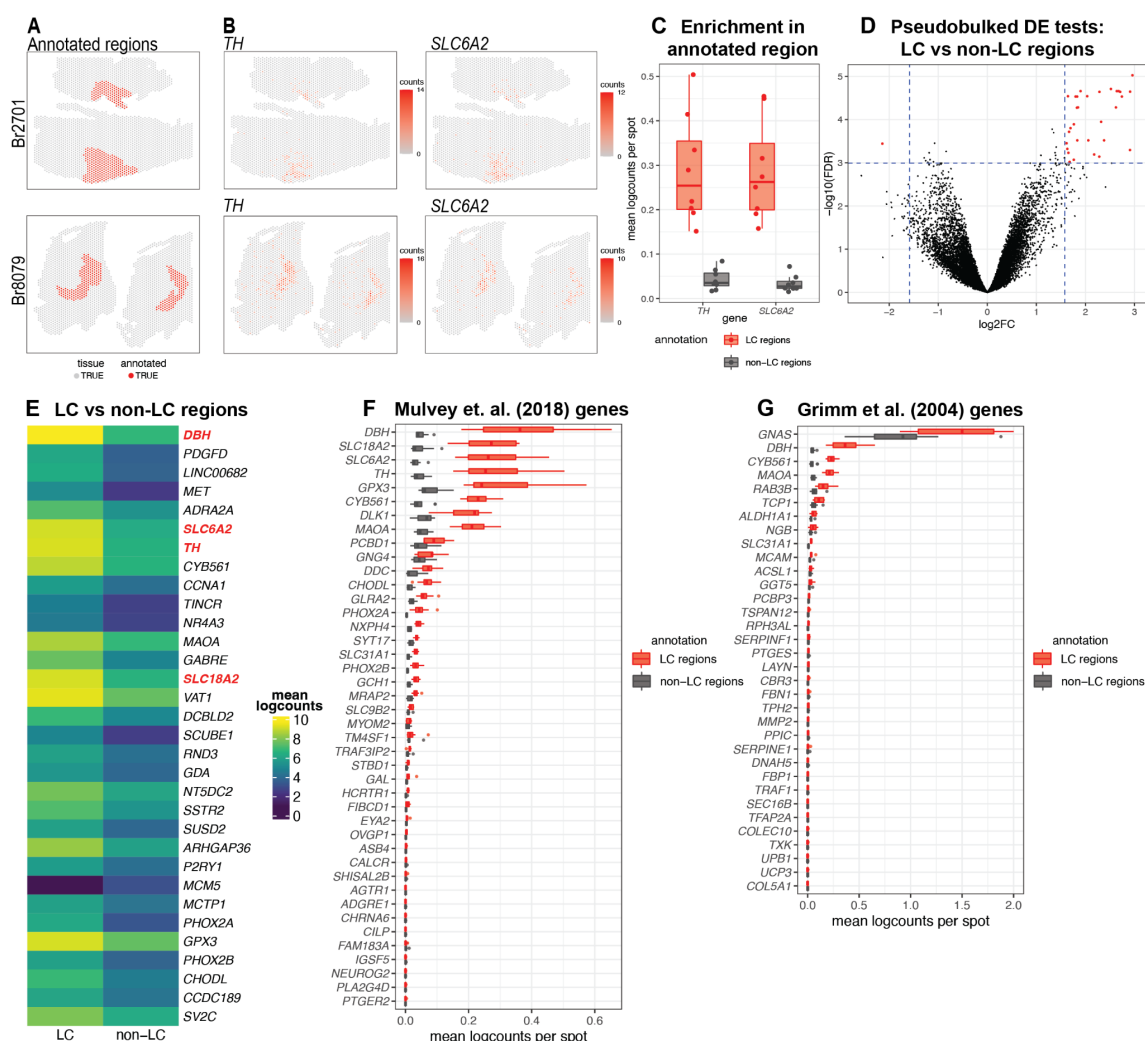
149

Figure 1: Experimental design to measure the landscape of gene expression in the postmortem human locus coeruleus (LC) using spatially-resolved transcriptomics (SRT) and single-nucleus RNA-sequencing (snRNA-seq). (A) Brainstem dissections at the level of the LC were conducted to collect tissue blocks from 5 neurotypical adult human brain donors. **(B)** Inclusion of the LC within the tissue sample block was validated using RNAscope [31,32] for a pan-neuronal marker gene (SNAP25) and two NE neuron-specific marker genes (TH and SLC6A2). High-resolution H&E stained histology images were acquired prior to SRT and snRNA-seq assays (scale bars: 2 mm in H&E stained image; 20 μ m in RNAscope images). **(C)** Prior to collecting tissue sections for SRT and snRNA-seq assays, tissue blocks were scored to enrich for the NE neuron-containing regions. For each sample, the LC region was manually annotated by visually identifying NE neurons in the H&E stained tissue sections. 100 μ m tissue sections from 3 of the same donors were used for snRNA-seq assays, which included FANS-based neuronal enrichment prior to library preparation to enrich for neuronal populations.

150 **Spatial gene expression in the human LC**

151 After applying the 10x Genomics Visium SRT platform [28], we executed several analyses to
152 characterize transcriptome-wide gene expression at spatial resolution within the human LC. First, we
153 manually annotated spots within regions identified as containing LC-NE neurons, based on
154 pigmentation, cell size, and morphology from the H&E stained histology images (**Figure 2A** and
155 **Supplementary Figure 1**). Next, we performed additional sample-level quality control (QC) on the
156 initial $N=9$ Visium capture areas (hereafter referred to as samples) by visualizing expression of two NE
157 neuron-specific marker genes (*TH* and *SLC6A2*) (**Figure 2B**), which identified one sample
158 (Br5459_LC_round2) without clear expression of these markers (**Supplementary Figure 2A-B**). This
159 sample was excluded from subsequent analyses, leaving $N=8$ samples from 4 out of the 5 donors. For
160 the $N=8$ Visium samples, the annotated regions were highly enriched in the expression of the NE
161 neuron marker genes (*TH* and *SLC6A2*) (**Figure 2C** and **Supplementary Figure 2C**), confirming that
162 these samples captured dense regions of LC-NE neurons within the annotated regions. We performed
163 spot-level QC to remove low-quality spots based on QC metrics previously applied to SRT data
164 [22,33,34] (**Methods**). Due to the large differences in read depth between samples (**Supplementary**
165 **Figure 3A**, **Supplementary Table 1**, **Methods**), we performed spot-level QC independently within
166 each sample. After filtering low-expressed genes (**Methods**), this resulted in a total of 12,827 genes
167 and 20,380 spots across the $N=8$ samples used for downstream analyses (**Supplementary Figure**
168 **3B**).

169
170 To investigate whether the LC regions could be annotated in a data-driven manner, we applied a
171 spatially-aware unsupervised clustering algorithm (BayesSpace [35]) after applying a batch integration
172 tool (Harmony [36]) to remove sample-specific technical variation in the molecular measurements
173 (**Supplementary Figure 4**). The spatially-aware clustering using $k=5$ clusters identified one cluster that
174 overlapped with the manually annotated LC regions in several samples. However, the proportion of
175 overlapping spots between the manually annotated LC region and this data-driven cluster (cluster 4,
176 colored red in **Supplementary Figure 5A**) was relatively low and varied across samples. We
177 quantitatively evaluated the clustering performance by calculating the precision, recall, F1 score, and
178 adjusted Rand index (ARI) for this cluster in each sample (see **Methods** for definitions). We found that
179 while precision was >0.8 in 3 out of 8 samples, recall was <0.4 in all samples, the F1 score was <0.6 in
180 all samples, and the ARI was <0.5 in all samples (**Supplementary Figure 5B**). Therefore, we judged
181 that the data-driven spatial domains identified from BayesSpace were not sufficiently reliable to use for
182 the downstream analyses, and instead proceeded with the histology-driven manual annotations for all
183 further analyses. In addition, we note that using the manual annotations avoids potential issues due to
184 inflated false discoveries resulting from circularity when performing differential gene expression testing
185 between sets of cells or spots defined by unsupervised clustering, when the same genes are used for
186 both clustering and differential testing [37]. Next, in addition to the manually annotated LC regions, we
187 also manually annotated a set of individual spots that overlapped with NE neuron cell bodies identified
188 within the LC regions, based on pigmentation, cell size, and morphology from the H&E histology
189 images (**Supplementary Figure 6A**). However, we observed relatively low overlap between spots with
190 expression of NE neuron marker genes and this second set of annotated individual spots. For example,
191 out of 706 annotated spots, only 331 spots had ≥ 2 observed UMI counts of *TH* (**Supplementary**
192 **Figure 6B**). We hypothesize that this may be due to technical factors including sampling variability in
193 the gene expression measurements, partial overlap between spots and cell bodies, potential diffusion
194 of mRNA molecules between spots, as well as biological variability in the expression of these marker
195 genes. Therefore, we instead used the LC region-level manual annotations for all further analyses.



196

197 **Figure 2: Spatial gene expression in the human LC using SRT.** (A) Spots within manually annotated LC
 198 regions containing NE neurons (red) and non-LC regions (gray), which were identified based on pigmentation, cell
 199 size, and morphology from the H&E stained histology images, from donors Br2701 (top row) and Br8079 (bottom
 200 row). (B) Expression of two NE neuron-specific marker genes (*TH* and *SLC6A2*). Color scale indicates unique
 201 molecular identifier (UMI) counts per spot. Additional samples corresponding to **A** and **B** are shown in
 202 **Supplementary Figures 1, 2A-B.** (C) Boxplots illustrating the enrichment in expression of two NE neuron-
 203 specific marker genes (*TH* and *SLC6A2*) in manually annotated LC regions compared to non-LC regions in the
 204 *N=8* Visium samples. Values show mean log-transformed normalized counts (logcounts) per spot within the
 205 regions per sample. Additional details are shown in **Supplementary Figure 2C.** (D) Volcano plot resulting from
 206 differential expression (DE) testing between the pseudobulked manually annotated LC and non-LC regions, which
 207 identified 32 highly significant genes (red) at a false discovery rate (FDR) significance threshold of 10^{-3} and
 208 expression fold-change (FC) threshold of 3 (dashed blue lines). Horizontal axis is shown on \log_2 scale and vertical
 209 axis on \log_{10} scale. Additional details and results for 437 statistically significant genes identified at an FDR
 210 threshold of 0.05 and an FC threshold of 2 are shown in **Supplementary Figure 7** and **Supplementary Table 2**.
 211 (E) Average expression in manually annotated LC and non-LC regions for the 32 genes from **D**. Color scale
 212 shows logcounts in the pseudobulked LC and non-LC regions averaged across *N=8* Visium samples. Genes are
 213 ordered in descending order by FDR (**Supplementary Table 2**). (F-G) Cross-species comparison showing
 214 expression of human ortholog genes for LC-associated genes identified in the rodent LC [25,26] using alternative
 215 experimental technologies. Boxplots show mean logcounts per spot in the manually annotated LC and non-LC
 216 regions per sample in the human data.

217 Next, to identify expressed genes associated with the LC regions, we performed differential expression
218 (DE) testing between the manually annotated LC and non-LC regions by pseudobulking spots, defined
219 as aggregating UMI counts from the combined spots within the annotated LC and non-LC regions in
220 each sample [22]. This analysis identified 32 highly significant genes at a false discovery rate (FDR)
221 threshold of 10^{-3} and expression fold-change (FC) threshold of 3 (**Figure 2D** and **Supplementary**
222 **Figure 7A**). This includes known NE neuron marker genes including *DBH* (the top-ranked gene by FDR
223 within this set), *SLC6A2* (ranked 6th), *TH* (ranked 7th), and *SLC18A2* (ranked 14th). Out of the 32
224 genes, 31 were elevated in expression within the LC regions, while one (*MCM5*) was depleted. The set
225 includes one long noncoding RNA (*LINC00682*), while the remaining 31 genes are protein-coding
226 genes (**Figure 2E** and **Supplementary Table 2**). Alternatively, using standard significance thresholds
227 of $\text{FDR} < 0.05$ and expression $\text{FC} > 2$, we identified a total of 437 statistically significant genes
228 (**Supplementary Figure 7B** and **Supplementary Table 2**).
229

230 As a second approach to identify genes associated with LC-NE neurons in an unsupervised manner,
231 we applied a method to identify spatially variable genes (SVGs), nnSVG [38]. This method ranks genes
232 in terms of the strength in the spatial correlation in their expression patterns across the tissue areas.
233 We ran nnSVG within each contiguous tissue area containing an annotated LC region for the $N=8$
234 Visium samples (total 13 tissue areas, where each Visium sample contains 1-3 tissue areas) and
235 combined the lists of top-ranked SVGs for the multiple tissue areas by averaging the ranks per gene. In
236 this analysis, we found that a subset of the top-ranked SVGs (11 out of the top 50) were highly-ranked
237 in samples from only one donor (Br8079), which we determined was due to the inclusion of a section of
238 the choroid plexus adjacent to the LC in these samples (based on expression of choroid plexus marker
239 genes including *CAPS* and *CRLF1*) (**Supplementary Figure 8A-C**). In order to focus on LC-associated
240 SVGs that were replicated across samples, we excluded the choroid plexus-associated genes by
241 calculating an overall average ranking of SVGs that were each included within the top 100 SVGs in at
242 least 10 out of the 13 tissue areas, which identified a list of 32 highly-ranked, replicated LC-associated
243 SVGs. These genes included known NE neuron marker genes (*DBH*, *TH*, *SLC6A2*, and *SLC18A2*) as
244 well as mitochondrial genes (**Supplementary Figure 8D**).
245

246 We also compared the expression of LC-associated genes previously identified in the rodent LC from
247 two separate studies. The first study used translating ribosomal affinity purification sequencing (TRAP-
248 seq) using an *SLC6A2* bacTRAP mouse line to identify gene expression profiles of the translatome of
249 LC neurons [25]. The second study used microarrays to assess gene expression patterns from laser-
250 capture microdissection of individual cells in tissue sections of the rat LC [26]. We converted the lists of
251 rodent LC-associated genes from these studies to human orthologs and calculated average expression
252 for each gene within the manually annotated LC and non-LC regions. A small number of genes from
253 both studies were highly associated with the manually annotated LC regions in the human data,
254 including *DBH*, *TH*, and *SLC6A2* from [25], and *DBH* and *GNAS* from [26]. However, the majority of the
255 genes from both studies were expressed at low levels in the human data, which may reflect species-
256 specific differences in biological function of these genes as well as differences due to the experimental
257 technologies employed (**Figure 2F-G**).
258
259

260 **Single-nucleus gene expression of NE neurons in the human LC**

261 To add cellular resolution to our spatial analyses, we characterized gene expression in the human LC
262 and surrounding region at single-nucleus resolution using the 10x Genomics Chromium single cell 3'
263 gene expression platform [29] in 3 of the same neurotypical adult donors from the SRT analyses.
264 Samples were enriched for NE neurons by scoring tissue blocks for the LC region and performing
265 FANS to enhance capture of neurons. After raw data processing, doublet removal using scDblFinder
266 [39], and standard QC and filtering, we obtained a total of 20,191 nuclei across the 3 samples (7,957,
267 3,015, and 9,219 nuclei respectively from donors Br2701, Br6522, and Br8079) (see **Supplementary**
268 **Table 1** for additional details). For nucleus-level QC processing, we used standard QC metrics
269 including the sum of UMI counts and detected genes [33] (see **Methods** for additional details). We
270 observed an unexpectedly high proportion of mitochondrial reads in nuclei with expression of NE
271 neuron marker genes (*DBH*, *TH*, and *SLC6A2*), which represented our rare population of interest, and
272 hence we did not remove nuclei based on proportion of mitochondrial reads (**Supplementary Figures**
273 **9-10**).

274

275 We identified NE neuron nuclei in the snRNA-seq data by applying an unsupervised clustering workflow
276 adapted from workflows used for snRNA-seq data in the human brain [23], using a two-stage clustering
277 algorithm consisting of high-resolution *k*-means and graph-based clustering that provides sensitivity to
278 identify rare cell populations [33]. The unsupervised clustering workflow identified 30 clusters, including
279 clusters representing major neuronal and non-neuronal cell populations, which we labeled based on
280 expression of known marker genes (**Figure 3A-B**). This included a cluster of NE neurons consisting of
281 295 nuclei (168, 4, and 123 nuclei from donors Br2701, Br6522, and Br8079, respectively), which we
282 identified based on expression of NE neuron marker genes (*DBH*, *TH*, and *SLC6A2*). In addition to the
283 NE neuron cluster, we identified clusters representing excitatory neurons, inhibitory neurons,
284 astrocytes, endothelial and mural cells, macrophages and microglia, oligodendrocytes, and
285 oligodendrocyte precursor cells (OPCs), as well as several clusters with ambiguous expression profiles
286 including pan-neuronal marker genes (*SNAP25* and *SYT1*), which may represent damaged neuronal
287 nuclei (**Figure 3A-B** and **Supplementary Figure 9**).

288

289 To validate the unsupervised clustering, we also applied a supervised strategy to identify NE neuron
290 nuclei by simply thresholding on expression of NE neuron marker genes (selecting nuclei with ≥ 1 UMI
291 counts of both *DBH* and *TH*). As described above, we noted a higher than expected proportion of
292 mitochondrial reads in nuclei with expression of *DBH* and *TH*, and did not filter on this parameter during
293 QC processing, in order to retain these nuclei (**Supplementary Figure 10A-B**). This supervised
294 approach identified 332 NE neuron nuclei (173, 4, and 155 nuclei from donors Br2701, Br6522, and
295 Br8079, respectively), including 188 out of the 295 NE neuron nuclei identified by unsupervised
296 clustering (**Supplementary Figure 10C**). We hypothesized that the differences for nuclei that did not
297 agree between the two approaches were due to sampling variability in the snRNA-seq measurements
298 for these two marker genes. To confirm this, we used an alternative method (smFISH RNAscope [32])
299 to assess co-localization of three NE neuron marker genes (*DBH*, *TH*, and *SLC6A2*) within individual
300 cells on additional tissue sections from one additional independent donor (Br8689). Visualization of
301 high-magnification confocal images demonstrated clear co-localization of these three marker genes
302 within individual cells (**Supplementary Figure 11**). Since the unsupervised clustering is based on
303 expression of a large number of genes and is therefore less sensitive to sampling variability for
304 individual genes, we used the unsupervised clustering results for all further downstream analyses.

305

306 We performed DE testing between the neuronal clusters and identified 327 statistically significant
307 genes with elevated expression in the NE neuron cluster, compared to all other neuronal clusters
308 captured in this region, at an FDR threshold of 0.05 and FC threshold of 2. These genes include known
309 NE neuron marker genes (*DBH*, *TH*, *SLC6A2*, and *SLC18A2*) as well as the 13 protein-coding
310 mitochondrial genes, which are highly expressed in large, metabolically active NE neurons (**Figure 3C**,
311 **Supplementary Figure 12A**, and **Supplementary Table 4**). Compared to the LC-associated genes
312 identified in the SRT samples, differences are expected since the snRNA-seq data contains
313 measurements from nuclei at single-nucleus resolution, while the SRT samples contain reads from
314 nuclei, cytoplasm, and cell processes from multiple cell populations within the annotated LC regions.
315

316 To compare with previous results in rodents, we evaluated the expression of the rodent LC marker
317 genes from [25,26] in the NE neuron cluster compared to all other neuronal clusters in the human
318 snRNA-seq data (**Figure 3D-E**). Consistent with the SRT samples, we observed that several genes
319 were conserved across species. However, compared to the SRT samples, we observed relatively
320 higher expression of the conserved genes within the NE neuron cluster, which is expected since the NE
321 neuron cluster contains reads from individual nuclei from this population only.
322

323 We note that a recent publication using snRNA-seq in mice found that LC-NE neurons were highly
324 enriched for *Calca*, *Cartpt*, *Gal*, and *Calcr* in addition to canonical NE neuron marker genes [27]. In the
325 human data, we noted significant enrichment of *GAL* and *CARTPT* in DE testing between the manually
326 annotated LC and non-LC regions in the SRT samples (**Supplementary Table 2**). While visualization
327 of the snRNA-seq clustering suggests that *CARTPT* is expressed in the NE neuron cluster in the
328 snRNA-seq data (**Supplementary Figure 13**), it was not identified as statistically significant in the DE
329 testing between the NE cluster compared to all other neuronal clusters (**Supplementary Table 4**). For
330 *CALCA* and *CALCR*, we observed no enrichment in the annotated LC regions in the SRT samples, nor
331 in the NE neuron cluster in the snRNA-seq data (**Supplementary Tables 2, 4** and **Supplementary**
332 **Figure 13**).
333

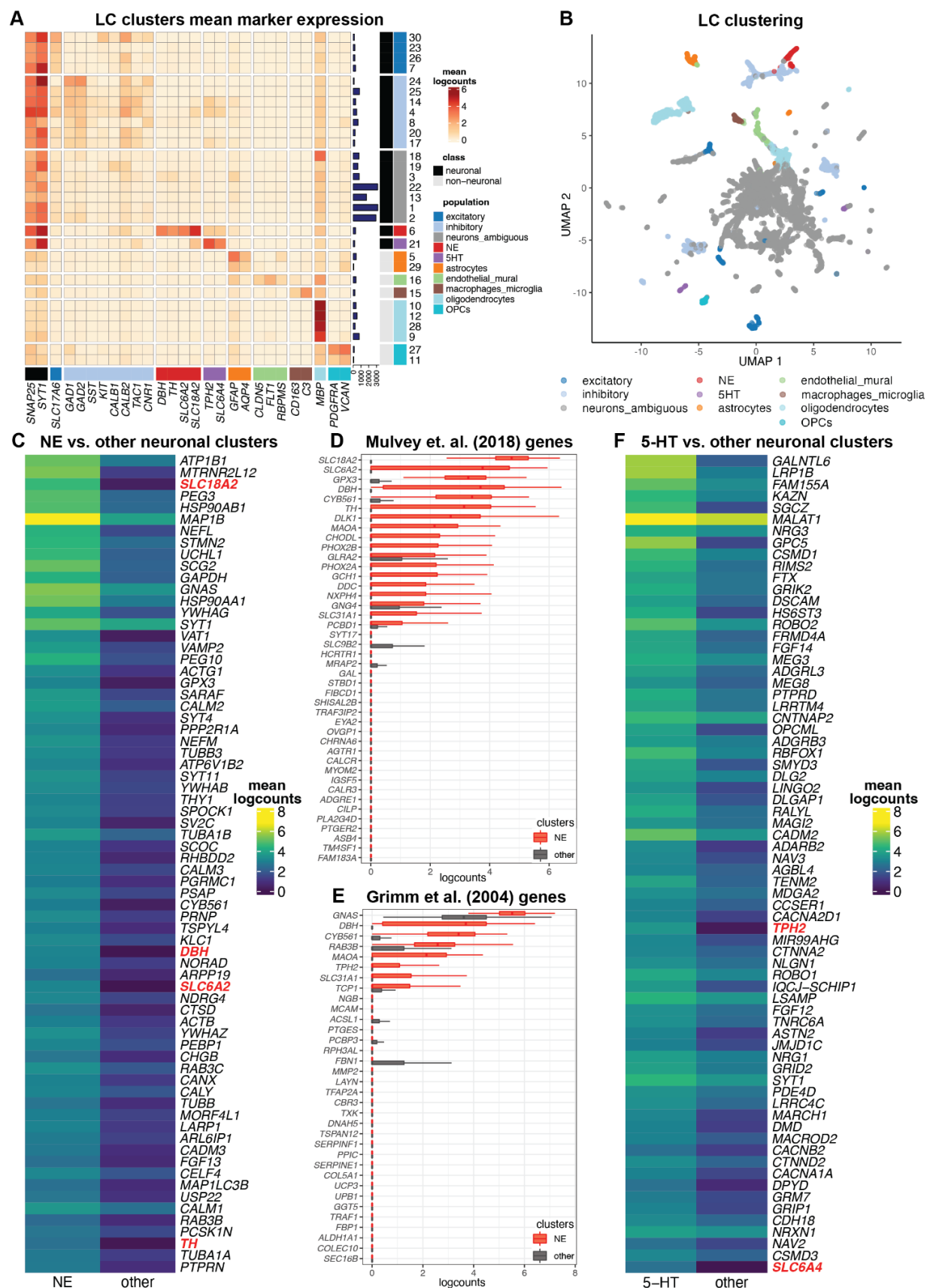
334 **Identification of 5-HT neurons and diversity of inhibitory neuron subpopulations in single- 335 nucleus data**

336 In addition to NE neurons, we identified a cluster of likely 5-hydroxytryptamine (5-HT, serotonin)
337 neurons in the unsupervised clustering analyses of the snRNA-seq data (**Figure 3A-B**) based on
338 expression of 5-HT neuron marker genes (*TPH2* and *SLC6A4*) [40]. This cluster consisted of 186 nuclei
339 (145, 28, and 13 nuclei from donors Br2701, Br6522, and Br8079, respectively). DE testing between
340 the neuronal clusters identified 361 statistically significant genes with elevated expression in the 5-HT
341 neuron cluster, compared to all other neuronal clusters captured in this region, at an FDR threshold of
342 0.05 and FC threshold of 2. These genes included the 5-HT neuron marker genes *TPH2* and *SLC6A4*
343 (**Figure 3F**, **Supplementary Figure 12B**, and **Supplementary Table 5**). To investigate the spatial
344 distribution of this population, we visualized the spatial expression of the 5-HT neuron marker genes
345 *TPH2* and *SLC6A4* in the *N=9* initial Visium samples, which showed that this population was distributed
346 across both the LC and non-LC regions (**Supplementary Figure 14A-B**). Similarly, we did not observe
347 significant spatial enrichment of *TPH2* and *SLC6A4* expression within the manually annotated LC
348 regions (**Supplementary Figure 14C**). To further confirm this finding, we applied RNAscope [32] to
349 visualize expression of an NE neuron marker gene (*TH*) and 5-HT neuron marker genes (*TPH2* and
350 *SLC6A4*) within additional tissue sections from donor Br6522, which demonstrated that the NE and 5-

351 HT marker genes were expressed within distinct cells and these neuronal populations were not
352 localized within the same regions (**Supplementary Figure 15**).
353
354 We also investigated the diversity of inhibitory neuronal subpopulations within the snRNA-seq data from
355 the human LC and surrounding region by applying a secondary round of unsupervised clustering to the
356 inhibitory neuron nuclei identified in the first round of clustering. This identified 14 clusters representing
357 inhibitory neuronal subpopulations, which varied in their expression of several inhibitory neuronal
358 marker genes including *CALB1*, *CALB2*, *TAC1*, *CNR1*, and *VIP* (additional marker genes shown in
359 **Supplementary Figures 13, 16**). In addition, similar to recently published results from mice [27], we
360 found that expression of neuropeptides *Pnoc*, *TAC1*, and *Penk* varied across the individual inhibitory
361 neuronal populations (**Supplementary Figure 13**).
362
363 In order to integrate the single-nucleus and spatial data, we also applied a spot-level deconvolution
364 algorithm, cell2location [41], to map the spatial coordinates of NE and 5-HT neurons within the Visium
365 samples. This algorithm integrates the snRNA-seq and SRT data by estimating the cell abundance of
366 the snRNA-seq populations, which are used as reference populations at cellular resolution, at each
367 spatial location (spot) in the Visium samples. This successfully mapped the NE neuron population from
368 the snRNA-seq data to the manually annotated LC regions in the Visium samples (**Supplementary**
369 **Figure 17A**). Similarly, for the 5-HT neurons, this population was mapped to the regions where this
370 population was previously identified based on expression of marker genes (**Supplementary Figure**
371 **17B**). However, the estimated absolute cell abundance of these neuronal populations per spot was
372 higher than expected, which may be due to their relatively large size and high transcriptional activity,
373 especially for NE neurons, compared to other neuronal and non-neuronal cell populations.
374

375 **Co-expression of cholinergic marker genes within NE neurons**

376 We observed expression of cholinergic marker genes, including *SLC5A7*, which encodes the high-
377 affinity choline transporter, and *ACHE*, within the NE neuron cluster in the snRNA-seq data
378 (**Supplementary Figure 13**). Because this result was unexpected, we experimentally confirmed co-
379 expression of *SLC5A7* transcripts with transcripts for NE neuron marker genes in individual cells using
380 RNAscope [32] on independent tissue sections from donors Br6522 and Br8079. We used RNAscope
381 probes for *SLC5A7* and *TH* (NE neuron marker), and imaged stained sections at 63x magnification to
382 generate high-resolution images, which allowed us to definitively localize expression of individual
383 transcripts within cell bodies. This confirmed co-expression of *SLC5A7* and *TH* in individual cells in a
384 tissue section from donor Br8079 (**Supplementary Figure 18**), validating that these transcripts are
385 expressed within the same cells. To further investigate the spatial distribution of the cholinergic marker
386 genes, we visualized expression of *SLC5A7* and *ACHE* in the Visium samples, which showed that
387 these genes were expressed both within and outside the annotated LC regions (**Supplementary**
388 **Figure 19**).
389
390



393 **Figure 3: Single-nucleus gene expression in the human LC using snRNA-seq.** We applied an unsupervised
394 clustering workflow to identify cell populations in the snRNA-seq data. **(A)** Unsupervised clustering identified 30
395 clusters representing populations including NE neurons (red), 5-HT neurons (purple), and other major neuronal
396 and non-neuronal cell populations (additional colors). Marker genes (columns) were used to identify clusters
397 (rows). Cluster IDs are shown in labels on the right, and numbers of nuclei per cluster are shown in horizontal
398 bars on the right. Heatmap values represent mean logcounts per cluster. **(B)** UMAP representation of nuclei, with
399 colors matching cell populations from heatmap. **(C)** DE testing between neuronal clusters identified a total of 327
400 statistically significant genes with elevated expression in the NE neuron cluster, at an FDR threshold of 0.05 and
401 FC threshold of 2. Heatmap displays the top 70 genes, ranked in descending order by FDR, excluding
402 mitochondrial genes, with NE neuron marker genes described in text highlighted in red. The full list of 327 genes
403 including mitochondrial genes is provided in **Supplementary Table 4**. Heatmap values represent mean logcounts
404 in the NE neuron cluster and mean logcounts per cluster averaged across all other neuronal clusters. **(D-E)**
405 Cross-species comparison showing expression of human ortholog genes for LC-associated genes identified in the
406 rodent LC [25,26] using alternative experimental technologies. Boxplots show logcounts per nucleus in the NE
407 neuron cluster and all other neuronal clusters. Boxplot whiskers extend to 1.5 times interquartile range, and
408 outliers are not shown. **(F)** DE testing between neuronal clusters identified a total of 361 statistically significant
409 genes with elevated expression in the 5-HT neuron cluster, at an FDR threshold of 0.05 and FC threshold of 2.
410 Heatmap displays the top 70 genes, ranked in descending order by FDR, with 5-HT neuron marker genes
411 described in text highlighted in red. The full list of 361 genes is provided in **Supplementary Table 5**.
412
413

414 **Interactive and accessible data resources**

415 We provide freely accessible data resources containing all datasets described in this manuscript, in the
416 form of both interactive web-accessible and downloadable resources (**Table 1**). The interactive
417 resources can be explored in a web browser via a Shiny [42] app for the Visium SRT data and an iSEE
418 [43] app for the snRNA-seq data (**Supplementary Figure 20**). The data resources are also available
419 from an R/Bioconductor ExperimentHub data package as downloadable objects in the
420 SpatialExperiment [44] and SingleCellExperiment [33] formats, which can be loaded in an R session
421 and contain meta-data including manual annotation labels and cluster labels.
422

Resource	Data	Format	Link
Shiny [42] web app	Visium SRT	Interactive web app	https://libd.shinyapps.io/locus-c_Visium/
iSEE [43] web app	snRNA-seq	Interactive web app	https://libd.shinyapps.io/locus-c_snRNA-seq/
R/Bioconductor ExperimentHub data package	Visium SRT and snRNA-seq	Downloadable R/Bioconductor objects in SpatialExperiment [44] and SingleCellExperiment [33] formats	https://bioconductor.org/packages/WeberDivechaL_Cdata (available in Bioconductor release version 3.16 from Nov 2, 2022 onwards)

423
424 **Table 1: Summary of data resources providing access to datasets described in this manuscript.** All
425 datasets described in this manuscript are freely accessible in the form of interactive web apps and downloadable
426 R/Bioconductor objects.
427
428

429 Discussion

430 Due to the small size and inaccessibility of the LC within the brainstem, this region has been relatively
431 understudied in the human brain, despite its involvement in numerous functions and disease
432 mechanisms. Our dataset provides the first transcriptome-wide characterization of the gene expression
433 landscape of the human locus coeruleus (LC) using spatially-resolved transcriptomics (SRT) and
434 single-nucleus RNA-sequencing (snRNA-seq). Analysis of these data identified a population of
435 norepinephrine (NE) neurons as well as a population of 5-hydroxytryptamine (5-HT, serotonin) neurons,
436 and spatially localized them within the LC and surrounding region. We evaluated expression of
437 previously known marker genes for these populations and identified novel sets of significant
438 differentially expressed (DE) genes, and assessed how their expression varies in space across the
439 neuroanatomy of the region. We compared our findings from the human LC to molecular profiles of LC
440 and peri-LC neurons that were previously characterized in rodents using alternative technological
441 platforms, which confirmed partial conservation of LC-associated genes across these species. Finally,
442 we validated our results using smFISH RNAscope to assess co-localization of marker genes on
443 independent tissue sections.

444
445 Identifying genes whose expression is enriched in NE neurons is important because the LC-NE system
446 is implicated in multiple neuropsychiatric and neurological disorders [4,8], and prominent loss of NE
447 cells in the LC occurs in neurodegenerative disorders [8–10]. Unbiased analysis of the snRNA-seq and
448 SRT data identified a number of genes that are enriched in the human LC region and in LC-NE neurons
449 themselves. As expected, these analyses validated enrichment of genes involved in NE synthesis and
450 packaging (*TH*, *SLC18A2*, *DBH*) as well as NE reuptake (*SLC6A2*). We also noted expression
451 selectively in LC-NE neurons of a number of genes whose expression is altered in animal models or in
452 human disease in the LC (*SSTR2*, *PHOX2A*, *PHOX2B*) [45,46]. We identified LC enrichment of a
453 number of genes that have been associated at the cellular level with apoptosis, cell loss, or pathology
454 in the context of neurodegeneration (*RND3*, *P2RY1*) [47–50]. We also noted enrichment of *NT5DC2* in
455 LC, a gene which has been associated with attention-deficit hyperactivity disorder (ADHD) and
456 regulates catecholamine synthesis *in vitro* [51,52]. Localization of these genes to the LC in humans,
457 and LC-NE neurons in particular, may provide important biological insights about physiological function
458 of these neurons and provide context about underlying mechanistic links between these genes and
459 disease risk. Future work using the transcriptome-wide molecular expression profiles of NE neurons at
460 single-nucleus resolution and the LC region at spatial resolution generated here could investigate
461 associations with individual genes and gene sets from genome-wide association studies (GWAS) for
462 these disorders as well as genes more generally associated with aging-related processes.

463
464 Our study has several limitations. The SRT data using the 10x Genomics Visium platform captures
465 around 1-10 cells per measurement location in the human brain, and future studies could apply a
466 higher-resolution platform to characterize expression at single-cell or sub-cellular spatial resolution. In
467 the single-nucleus data, we identified a relatively small number of NE neurons, which may be related to
468 technical factors that affect the recovery of this population due to their relatively large size and fragility.
469 These technical factors may have also contributed to the unexpectedly high proportion of mitochondrial
470 reads that we observed in NE neurons in the snRNA-seq data. While mitochondrial reads are not
471 expected in the nuclear compartment, recent studies reported contamination of nuclear preparations in
472 snRNA-seq data with ambient mRNAs from abundant cellular transcripts [53]. Given the relatively
473 elevated energy demand and increased metabolic activity of NE neurons, higher than expected

474 mitochondrial contamination in the nuclear preparation of LC tissue may be plausible. Because NE
475 neurons were the population of highest interest to profile in this dataset, we opted not to perform QC
476 filtering on the proportion of mitochondrial reads, in order to retain this population. Further optimizing
477 technical procedures for cell sorting and cryosectioning to avoid cellular damage, as well as for
478 straining for large cells, could enhance recovery of this population for future, larger-scale snRNA-seq
479 studies in this brain region.

480
481 Since the identification of 5-HT neurons in the single-nucleus data was an unexpected finding, the
482 experimental procedures were not designed to optimally recover this population, and the precise
483 anatomical origin of the 5-HT neurons recovered in this dataset is not entirely clear. It is possible that
484 these cells were close to the borders of the LC dissections, residing within the dorsal raphe nucleus,
485 which is neuroanatomically adjacent to the LC. Supporting this hypothesis, RNAscope data in
486 **Supplementary Figure 15** from an independent tissue section shows that *TPH2* and *SLC6A4*
487 expression appears to be distinct from the LC region containing a high density of NE cells. However,
488 there is some evidence for expression of serotonergic markers within the LC region in rodents
489 [26,54,55], and our SRT data does support this possibility in the human brain, although further
490 characterization is needed. Comprehensively understanding the full molecular diversity of 5-HT
491 neurons in the human brain would require dissections that systematically sample across the extent of
492 the dorsal raphe nucleus. Similarly, the identification of cholinergic marker gene expression, particularly
493 the robust expression of *SLC5A7* within NE neurons, was unexpected. While previous studies have
494 identified small populations of cholinergic interneurons within or adjacent to the LC in rodents [27],
495 analysis of our data did not classify any of the other neuronal populations as cholinergic per se.
496 However, both the SRT and RNAscope data (**Supplementary Figure 18**) supports the hypothesis that
497 expression of cholinergic markers occurs in NE cells themselves, as well as in sparse populations of
498 cholinergic neurons adjacent to the LC region that do not express NE marker genes. We note that our
499 snRNA-seq data may be underpowered to fully identify and classify these sparse populations, and
500 future experiments designed to specifically investigate this finding in more detail could lead to a better
501 understanding of cholinergic signaling within the LC of the human brain. Similarly, our snRNA-seq may
502 be underpowered to perform gene set enrichment studies [56] to identify whether the NE and 5-HT
503 neurons harbor aggregated genetic risk for psychiatric disorders, but these data could be aggregated
504 with future snRNA-seq data generated from the LC to address this question. To facilitate further
505 exploration of these data, we provide a freely accessible data resource that includes the snRNA-seq
506 and SRT data in both web-based and R-based formats, as well as reproducible code for the
507 computational analysis workflows for the snRNA-seq and SRT data.

508
509

510 Materials and Methods

511 Postmortem human brain tissue samples for RNAscope, SRT, and snRNA-seq assays

512 Brain donations in the Lieber Institute for Brain Development (LIBD) Human Brain Repository were
513 collected from the Office of the Chief Medical Examiner of the State of Maryland under the Maryland
514 Department of Health's IRB protocol #12-24, and from the Western Michigan University Homer Stryker
515 MD School of Medicine, Department of Pathology, and the Department of Pathology, University of
516 North Dakota School of Medicine and Health Sciences, both under WCG IRB protocol #20111080.
517 Clinical characterization, diagnoses, and macro- and microscopic neuropathological examinations were
518 performed on all samples using a standardized paradigm, and subjects with evidence of macro- or
519 microscopic neuropathology were excluded. Details of tissue acquisition, handling, processing,
520 dissection, clinical characterization, diagnoses, neuropathological examinations, RNA extraction, and
521 quality control measures have been described previously [57,58]. We obtained tissue blocks from 5
522 male neurotypical brain donors of European ancestry. To select tissue blocks for study inclusion, we
523 identified the LC in transverse slabs of the pons from fresh-frozen human brain. The LC was identified
524 through visual inspection of the slab, based on neuroanatomical landmarks and the presence of
525 neuromelanin pigmentation. For each donor, a tissue block was dissected from the dorsal aspect of the
526 pons, centered around the LC, using a dental drill. The tissue block was taken at the level of the motor
527 trigeminal nucleus and superior cerebellar peduncle. Tissue blocks were kept at -80 °C until sectioning
528 for experiments. We cut 10 µm tissue sections for performing SRT assays using the 10x Genomics
529 Visium SRT platform [28]. High-resolution images of the H&E stained histology were acquired prior to
530 on-slide cDNA synthesis and completing the Visium assays. Assays were performed on 2-4 tissue
531 sections collected from each of the 5 donors, and the tissue blocks were scored to fit 2-3 tissue
532 sections from the same donor onto a single Visium capture area to maximize the use of the Visium
533 slides. This resulted in a total of $N=9$ Visium capture areas (hereafter referred to as samples) in the
534 SRT dataset. For 3 of the 5 donors, we cut additional 100 µm cryosections for snRNA-seq assays using
535 the 10x Genomics Chromium snRNA-seq platform [29]. **Supplementary Table 1** provides information
536 on brain donor demographics as well as sample information for the SRT and snRNA-seq datasets.

537 Multiplexed smFISH using RNAscope

538 For RNAscope experiments, tissue blocks were sectioned at 10 µm and single-molecule fluorescent *in*
539 *situ* hybridization assays were performed with RNAscope technology [32] using the Fluorescent
540 Multiplex Kit v.2 and 4-plex Ancillary Kit (catalog no. 323100, 323120 ACD) according to the
541 manufacturer's instructions. Briefly, 10 µm tissue sections (2-4 sections per donor) were fixed with 10%
542 neutral buffered formalin solution (catalog no. HT501128, Sigma-Aldrich) for 30 min at room
543 temperature, series dehydrated in increasing concentrations of ethanol (50%, 70%, 100%, and 100%),
544 pretreated with hydrogen peroxide for 10 min at room temperature and treated with protease IV for
545 30 min. For QC experiments to confirm LC inclusion in the tissue block (**Figure 1B** showing example for
546 additional independent donor Br8689), tissue sections were incubated with 3 different probes (2 LC-NE
547 neuron markers and one pan-neuronal marker): *SLC6A2* (catalog no. 526801-C1, Advanced Cell
548 Diagnostics) encoding the norepinephrine transporter, *TH* (catalog no. 441651-C2, Advanced Cell
549 Diagnostics) encoding tyrosine hydroxylase, and *SNAP25* (catalog no. 518851-C3, Advanced Cell
550 Diagnostics). To confirm co-expression of LC-NE marker genes within individual cells (**Supplementary**
551 **Figure 11**), we used *SLC6A2* (catalog no. 526801-C1, Advanced Cell Diagnostics), *TH* (catalog no.
552 441651-C2, Advanced Cell Diagnostics), and *DBH* (catalog no. 545791-C3, Advanced Cell

553 Diagnostics) encoding dopamine beta-hydroxylase. To localize serotonergic and cholinergic markers
554 within the LC (**Supplementary Figure 15**), we used *TH* (catalog no. 441651-C2, Advanced Cell
555 Diagnostics) encoding tyrosine hydroxylase, *TPH2* (catalog no. 471451-C1, Advanced Cell
556 Diagnostics) encoding tryptophan hydroxylase 2, *SLC6A4* (catalog no. 604741-C3, Advanced Cell
557 Diagnostics) encoding the serotonin transporter, and *SLC5A7* (catalog no. 564671-C4, Advanced Cell
558 Diagnostics) encoding the high-affinity choline transporter. After probe labeling, sections were stored
559 overnight in 4x saline-sodium citrate buffer (catalog no. 10128-690, VWR). After amplification steps
560 (AMP1-3), probes were fluorescently labeled with Opal Dyes 520, 570, and 690 (catalog no.
561 FP1487001KT, FP1488001KT, and FP1497001KT, Akoya Biosciences; 1:500 dilutions for all the dyes)
562 and counter-stained with DAPI (4',6-diamidino-2-phenylindole) to label cell nuclei. Lambda stacks were
563 acquired in z-series using a Zeiss LSM780 confocal microscope equipped with 20x, 0.8 numerical
564 aperture (NA) and 63x, 1.4 NA objectives, a GaAsP spectral detector, and 405-, 488-, 561- and 633-nm
565 lasers. All lambda stacks were acquired with the same imaging settings and laser power intensities.
566 After image acquisition, lambda stacks in z-series were linearly unmixed using Zen Black (weighted; no
567 autoscale) using reference emission spectral profiles previously created in Zen for the dotdotdot
568 software (git hash v.4e1350b) [31], stitched, maximum intensity projected, and saved as Carl Zeiss
569 Image (.czi) files.

570 **Visium SRT with H&E staining data generation and sequencing**

571 Tissue blocks were embedded in OCT medium and cryosectioned at 10 µm on a cryostat (Leica
572 Biosystems). Briefly, Visium Gene Expression Slides were cooled inside the cryostat and tissue
573 sections were then adhered to the slides. Tissue sections were fixed with methanol and then stained
574 with hematoxylin and eosin (H&E) according to manufacturer's staining and imaging instructions (User
575 guide CG000160 Rev C). Images of the H&E stained slides were acquired using a CS2 slide scanner
576 (Leica Biosystems) equipped with a color camera and a 20x, 0.75 NA objective and saved as a Tagged
577 Image File (.tif). Following H&E staining and acquisition of images, slides were processed for the
578 Visium assay according to manufacturer's reagent instructions (Visium Gene Expression protocol User
579 guide CG000239, Rev D) as previously described [22]. In brief, the workflow includes permeabilization
580 of the tissue to allow access to mRNA, followed by reverse transcription, removal of cDNA from the
581 slide, and library construction. Tissue permeabilization experiments were conducted on a single LC
582 sample used in the study and an optimal permeabilization time of 18 minutes was identified and used
583 for all sections across donors. Sequencing libraries were quality controlled and then sequenced on the
584 MiSeq, NextSeq, or NovaSeq Illumina platforms. Sequencing details and summary statistics for each
585 sample are reported in **Supplementary Table 1**.

586 **snRNA-seq data generation and sequencing**

587 Following SRT data collection, three tissue blocks (Br6522, Br8079, and Br2701) were used for snRNA-
588 seq. Prior to tissue collection for snRNA-seq assays, tissue blocks were further scored based on the
589 RNAscope and SRT data to enrich tissue collection to the localized site of LC-NE neurons. After
590 scoring the tissue blocks, samples were sectioned at 100 µm and collected in cryotubes. The sample
591 collected for Br6522 contained 10 sections, weighing 51 mg, and the samples from Br8079 and Br2701
592 each contained 15 sections, weighing 60.9 mg and 78.9 mg, respectively. These samples were
593 processed following a modified version of the 'Frankenstein' nuclei isolation protocol as previously
594 described [23]. Specifically, chilled EZ lysis buffer (MilliporeSigma) was added to the LoBind
595 microcentrifuge tube (Eppendorf) containing cryosections, and the tissue was gently broken up, on ice,

596 via pipetting. This lysate was transferred to a chilled dounce, rinsing the tube with additional EZ lysis
597 buffer. The tissue was then homogenized using part A and B pestles, respectively, for ~10 strokes,
598 each, and the homogenate was strained through a 70 μ m cell strainer. After lysis, the samples were
599 centrifuged at 500 g at 4 °C for 5 min, supernatant was removed, then the sample was resuspended in
600 EZ lysis buffer. Following a 5 min incubation, samples were centrifuged again. After supernatant
601 removal, wash/resuspension buffer (PBS, 1% BSA, and 0.2 U/uL RNasin), was gently added to the
602 pellet for buffer interchange. After a 5 min incubation, each pellet was again washed, resuspended and
603 centrifuged three times.

604

605 For staining, each pellet was resuspended in a wash/resuspension buffer with 3% BSA, and stained
606 with AF488-conjugated anti-NeuN antibody (MiliporeSigma, catalog no. MAB377X), for 30 min on ice
607 with frequent, gentle mixing. After incubation, these samples were washed with 1 mL
608 wash/resuspension buffer, then centrifuged, and after the supernatant was aspirated, the pellet was
609 resuspended in wash/resuspension buffer with propidium iodide (PI), then strained through a 35 μ m cell
610 filter attached to a FACS tube. Each sample was then sorted on a Bio-Rad S3e Cell Sorter on 'Purity'
611 mode into a 10x Genomics reverse transcription mix, without enzyme. A range of 5637-9000 nuclei
612 were sorted for each sample, aiming for an enrichment of ~60% singlet, NeuN+ nuclei. Then the 10x
613 Chromium reaction was completed following the Chromium Next GEM Single Cell 3' Reagent Kits v3.1
614 (Dual Index) revision A protocol, provided by the manufacturer (10x Genomics) to generate libraries for
615 sequencing. The number of sequencing reads and platform used per sample are shown in
616 **Supplementary Table 1**.

617 Analysis of Visium SRT data

618 This section describes additional details on the computational analyses of the Visium SRT data that are
619 not included in the main text.

620

621 Manual alignment of the H&E stained histology images to the expression spot grid was performed using
622 the 10x Genomics Loupe Browser software (v. 5.1.0). The raw sequencing data files (FASTQ files) for
623 the sequenced library samples were processed using the 10x Genomics Space Ranger software (v.
624 1.3.0) [59] using the human genome reference transcriptome version GRCh38 2020-A (July 7, 2020)
625 provided by 10x Genomics. Sequencing summary statistics for each sample are provided in
626 **Supplementary Table 1**.

627

628 For spot-level QC filtering, we removed outlier spots that were more than 3 median absolute deviations
629 (MADs) above or below the median sum of UMI counts or the median number of detected genes per
630 spot [33]. We did not use the proportion of mitochondrial reads per spot for spot-level QC filtering, since
631 we observed a high proportion of mitochondrial reads in the NE nuclei in the snRNA-seq data (for more
632 details, see **Results** and **Supplementary Figure 9**), so using this QC metric would risk removing the
633 rare population of NE nuclei of interest in the snRNA-seq data. Therefore, for consistency with the
634 snRNA-seq analyses, we did not use the proportion of mitochondrial reads for spot-level QC filtering in
635 the SRT data. Due to the large differences in read depth between samples (e.g. median sum of UMI
636 counts ranged from 118 for sample Br6522_LC_2_round1 to 2,252 for sample Br6522_LC_round3; see
637 **Supplementary Figure 3A** and **Supplementary Table 1** for additional details), we performed spot-
638 level QC independently within each sample. The spot-level QC filtering identified a total of 287 low-
639 quality spots (1.4% out of 20,667 total spots) from the N=8 Visium samples that passed sample-level
640 QC. These spots were removed from subsequent analyses (**Supplementary Figure 3B**). For gene-

641 level QC filtering, we removed low-expressed genes with a total of less than 80 UMI counts summed
642 across the $N=8$ Visium samples.

643
644 For the evaluation of the spatially-aware clustering with BayesSpace [35] to identify the LC regions in a
645 data-driven manner, precision is defined as the proportion of spots in the selected cluster that are from
646 the true annotated LC region, recall is defined as the proportion of spots in the true annotated LC
647 region that are in the selected cluster, F1 score is defined as the harmonic mean of precision and recall
648 (values ranging from 0 to 1, with 1 representing perfect accuracy), and the adjusted Rand index is
649 defined as the percentage of correct assignments, adjusted for chance (values ranging from 0 for
650 random assignment to 1 for perfect assignment).

651
652 For the pseudobulked DE testing, we aggregated the reads within the LC and non-LC regions using the
653 scater package [60], and then used the limma package [61] to calculate empirical Bayes moderated DE
654 tests.

655 Analysis of snRNA-seq data

656 This section describes additional details on the computational analyses of the snRNA-seq data that are
657 not included in the main text.

658
659 We aligned sequencing reads using the 10x Genomics Cell Ranger software [62] (version 6.1.1,
660 cellranger count, with option --include-introns), using the human genome reference transcriptome
661 version GRCh38 2020-A (July 7, 2020) provided by 10x Genomics. We called nuclei (distinguishing
662 barcodes containing nuclei from empty droplets) using Cell Ranger (“filtered” outputs), which recovered
663 8,979, 3,220, and 10,585 barcodes for donors Br2701, Br6522, and Br8079, respectively. We applied
664 scDblFinder [39] using default parameters to computationally identify and remove doublets, which
665 removed 1,022, 205, and 1,366 barcodes identified as doublets for donors Br2701, Br6522, and
666 Br8079, respectively.

667
668 We performed nucleus-level QC processing by defining low-quality nuclei as nuclei with outlier values
669 more than 3 median absolute deviations (MADs) above or below the median sum of UMI counts or the
670 median number of detected genes [33], which did not identify any low-quality nuclei, so all nuclei were
671 retained. We did not use the proportion of mitochondrial reads for QC processing, since we observed a
672 high proportion of mitochondrial reads in nuclei with expression of NE neuron markers (*DBH* and *TH*)
673 (for more details, see **Results** and **Supplementary Figure 10**). Therefore, QC filtering on the
674 proportion of mitochondrial reads would risk removing the rare population of NE neuron nuclei of
675 interest. We performed gene-level QC filtering by removing low-expressed genes with less than 30 UMI
676 counts summed across all nuclei. After doublet removal and QC processing, we obtained a total of
677 7,957, 3,015, and 9,219 nuclei from donors Br2701, Br6522, and Br8079, respectively.

678
679 For the unsupervised clustering, we used a two-stage clustering algorithm consisting of high-resolution
680 *k*-means and graph-based clustering that provides sensitivity to identify rare cell populations [33]. For
681 the first round of clustering (results in **Figure 3A-B, Supplementary Figure 13**), we used 2,000
682 clusters for the *k*-means step, and 10 nearest neighbors and Walktrap clustering for the graph-based
683 step. For the secondary clustering of inhibitory neurons (**Supplementary Figure 16**), we used 1,000
684 clusters for the *k*-means step, and 10 nearest neighbors and Walktrap clustering for the graph-based
685 step. We did not perform any batch integration prior to clustering, since batch integration algorithms

686 may strongly affect rare populations but these algorithms have not yet been independently evaluated
687 on datasets with rare populations (<1% of cells). We calculated highly variable genes, log-transformed
688 normalized counts (logcounts), and performed dimensionality reduction using the scater and scran
689 packages [34,60].
690

691 For the DE testing, we performed pairwise DE testing between all neuronal clusters, using the
692 findMarkers() function from the scran package [34]. We tested for genes with \log_2 -fold-changes
693 (\log_2FC) significantly greater than 1 (lfc = 1, direction = “up”) to identify genes with elevated expression
694 in any of the neuronal clusters compared to all other neuronal clusters.
695

696 For the spot-level deconvolution using cell2location [41], we used the following parameters for human
697 brain data from the Visium platform: detection_alpha = 20, N_cells_per_location = 3.
698
699

700 Supplementary Tables

701

702 **Supplementary Table 1: Summary of experimental design, sample information, and donor**
703 **demographic details.** Information includes the types of assays performed, donor demographic details,
704 sample IDs, number of Visium tissue areas per sample, and sequencing summary statistics for each
705 sample. The table is provided as an .xlsx file.

706

707 **Supplementary Table 2: Differential expression (DE) testing results in pseudobulked Visium**
708 **SRT data.** Columns include gene ID, gene name, mean log-transformed normalized counts (logcounts)
709 in manually annotated LC and non-LC regions (“mean_logcounts_LC” and “mean_logcounts_nonLC”),
710 log₂ fold change (log₂FC), p-value, false discovery rate (FDR), and columns identifying significant (FDR
711 < 0.05 and FC > 2) and highly significant (FDR < 10⁻³ and FC > 3) genes. The table is provided as a
712 .csv file.

713

714 **Supplementary Table 3: Spatially variable genes (SVGs) in Visium SRT data.** Results for SVGs
715 identified using nnSVG in Visium SRT data. Columns include gene ID, gene name, overall rank of
716 SVGs identified in replicated tissue areas (“replicated_overall_rank”, i.e. top LC-associated SVGs; see
717 **Results**), overall rank of identified SVGs according to average rank across tissue areas (“overall_rank”,
718 i.e. including choroid plexus-associated SVGs from one donor; see **Results**), average rank of identified
719 SVGs across individual tissue areas (“average_rank”), number of times (tissue areas) identified within
720 top 100 SVGs (“n_withinTop100”), and ranks within each individual tissue area. The table is provided
721 as a .csv file.

722

723 **Supplementary Table 4: Differential expression (DE) testing results for NE neuron cluster in**
724 **snRNA-seq data.** DE testing results comparing NE neuron cluster against all other neuronal clusters in
725 snRNA-seq data. Columns include gene ID, gene name, sum of UMI counts across all nuclei
726 (“sum_gene”), average log-transformed normalized counts (logcounts) within the NE neuron cluster
727 (“self_average”), average of average logcounts within all other neuronal clusters (“other_average”),
728 combined p-value, false discovery rate (FDR), summary log₂ fold change in the pairwise comparison
729 with the lowest p-value (“summary_logFC”), and column identifying significant (FDR < 0.05 and FC > 2)
730 genes. The table is provided as a .csv file.

731

732 **Supplementary Table 5: Differential expression (DE) testing results for 5-HT neuron cluster in**
733 **snRNA-seq data.** DE testing results comparing 5-HT neuron cluster against all other neuronal clusters
734 in snRNA-seq data. Columns include gene ID, gene name, sum of UMI counts across all nuclei
735 (“sum_gene”), average log-transformed normalized counts (logcounts) within the 5-HT neuron cluster
736 (“self_average”), average of average logcounts within all other neuronal clusters (“other_average”),
737 combined p-value, false discovery rate (FDR), summary log₂ fold change in the pairwise comparison
738 with the lowest p-value (“summary_logFC”), and column identifying significant (FDR < 0.05 and FC > 2)
739 genes. The table is provided as a .csv file.

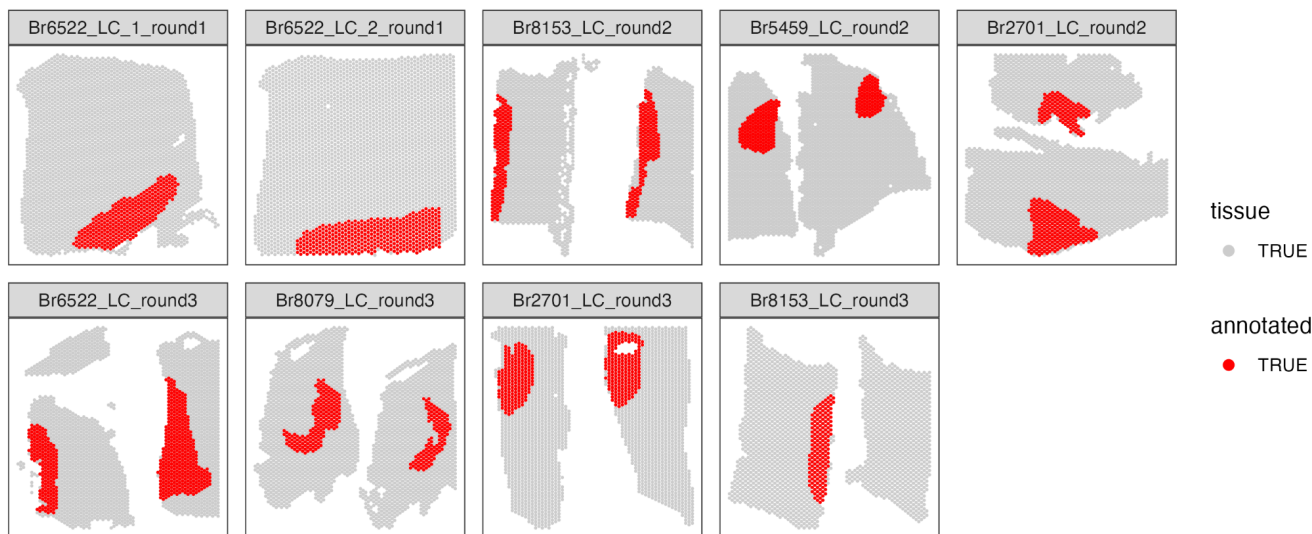
740

741

742 Supplementary Figures

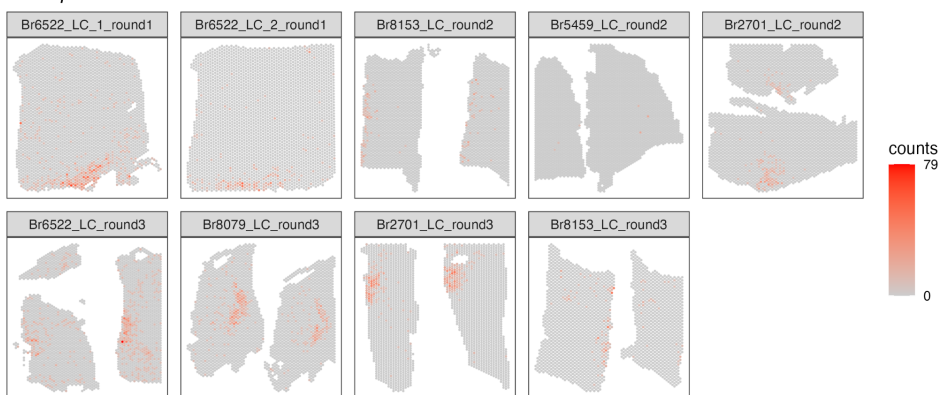
743

Annotations



753

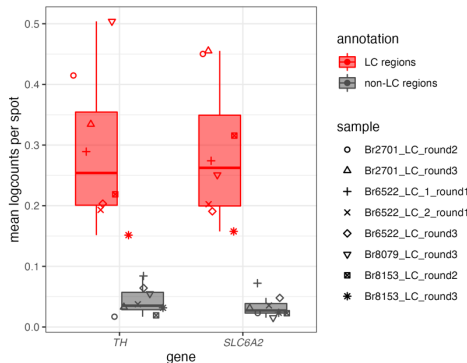
A TH expression



B SLC6A2 expression



C Enrichment



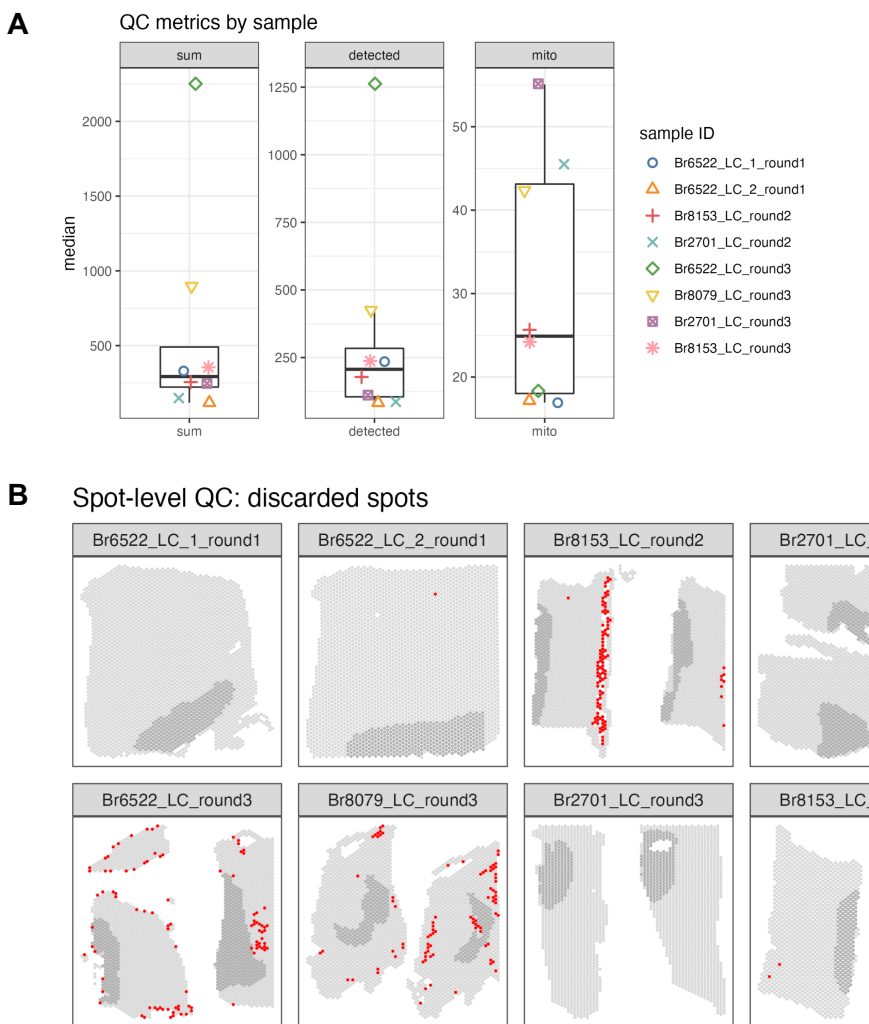
754

755 **Supplementary Figure 2: Spatial expression of two NE neuron-specific marker genes in Visium samples**
756 **for quality control (QC) in SRT data. (A-B)** Spot-plot visualizations of NE neuron marker gene expression (*TH*
757 and *SLC6A2*, **A** and **B**, respectively) in the $N=9$ Visium samples. Color scale shows UMI counts per spot. One
758 sample (Br5459_LC_round2) did not show clear expression of the NE neuron marker genes. This sample was
759 excluded from subsequent analyses, leaving $N=8$ Visium capture areas (samples) from 4 out of the 5 donors. **(C)**
760 Enrichment of NE neuron marker gene expression (*TH* and *SLC6A2*) within manually annotated LC regions
761 compared to non-LC regions in the $N=8$ Visium samples. Boxplots show values as mean log-transformed
762 normalized counts (logcounts) per spot within each region per sample, with samples represented by shapes.

763

764

765



766

767

768

769

770

771

772

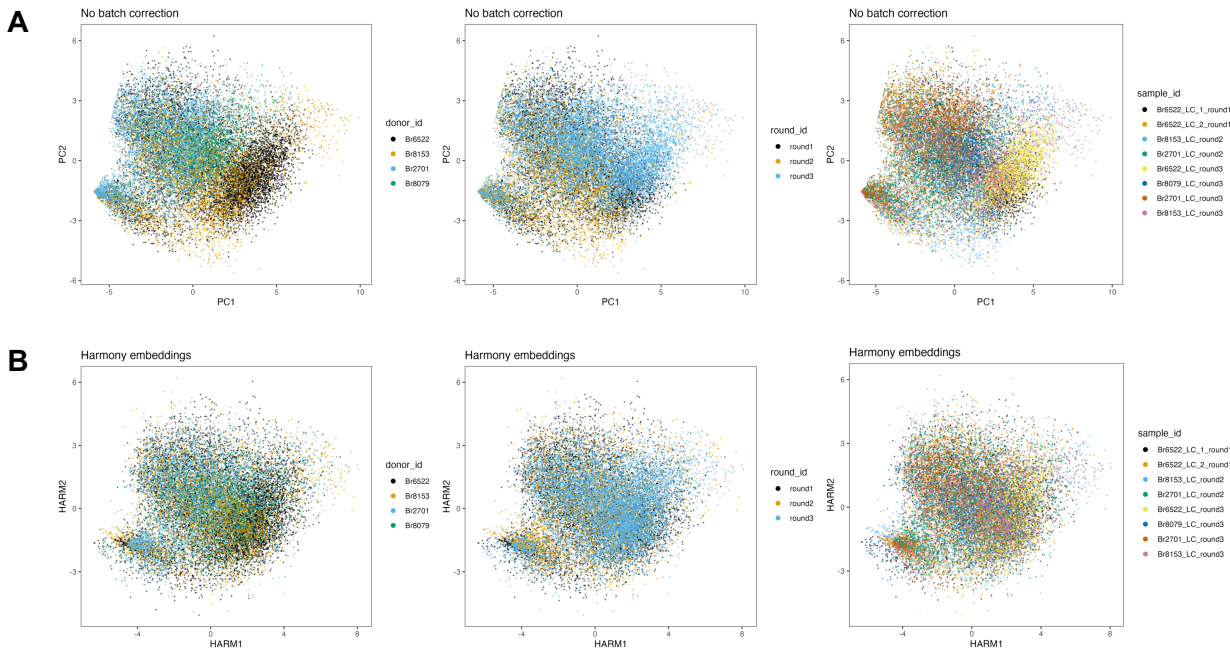
773

774

775

Supplementary Figure 3: Spot-level quality control (QC) data visualizations for Visium samples in SRT data. (A) QC metrics, medians per sample (from left to right: sum of UMI counts per spot, number of detected genes per spot, and proportion of mitochondrial reads per spot). Boxplots show median for each QC metric per sample, with samples represented by shapes. **(B)** Applying thresholds of 3 median absolute deviations (MADs) to the sum of UMI counts and number of detected genes for each sample identified a total of 287 low-quality spots (red) (1.4% out of 20,667 total spots), which were removed from subsequent analyses. We did not use the proportion of mitochondrial reads for spot-level QC filtering (see **Methods** for more details).

776



777

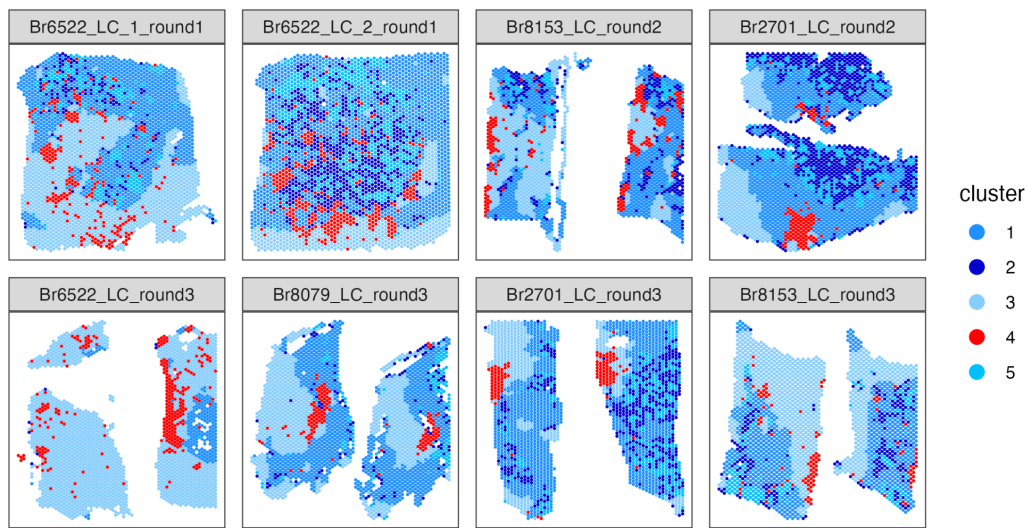
778 **Supplementary Figure 4: Dimensionality reduction embeddings before and after batch integration across**
779 **Visium samples in SRT data.** We applied a batch integration tool (Harmony [36]) to remove technical variation in
780 the molecular measurements between the $N=8$ Visium samples from 4 donors. The integrated measurements
781 were subsequently used as the input for spatially-aware clustering using BayesSpace [35]. **(A)** Principal
782 component analysis (PCA) (top 2 PCs) calculated on molecular expression measurements, with spots labeled
783 (left to right) by donor ID, round ID, and sample ID, without applying any batch integration. **(B)** Harmony
784 embeddings (top 2 Harmony embedding dimensions) after applying Harmony batch integration on sample IDs,
785 with spots labeled (left to right) by donor ID, round ID, and sample ID, demonstrating that the technical variation
786 has been reduced.

787

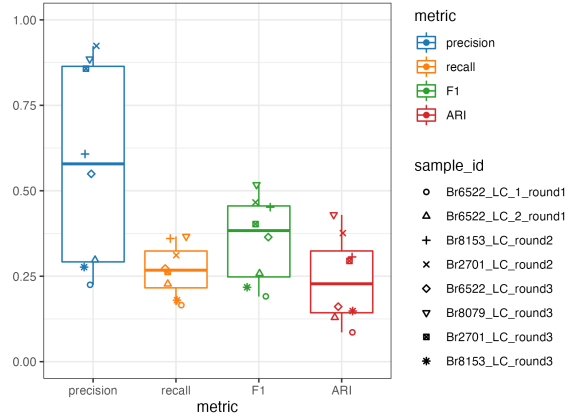
788

789

A BayesSpace clustering



B Spatially-aware clustering performance



790

791

Supplementary Figure 5: Identifying LC and non-LC regions in a data-driven manner by spatially-aware unsupervised clustering in SRT data. We applied a spatially-aware unsupervised clustering algorithm (BayesSpace [35]) to investigate whether the LC and non-LC regions in each Visium sample could be annotated in a data-driven manner. **(A)** Using BayesSpace with $k=5$ clusters, we clustered spots from the $N=8$ Visium samples using the Harmony batch-integrated molecular measurements. Cluster 4 (red) corresponds most closely to the manually annotated LC regions. **(B)** BayesSpace clustering performance evaluated in terms of concordance between cluster 4 (red) and the manually annotated LC region in each sample. Clustering performance was evaluated in terms of precision, recall, F1 score, and adjusted Rand index (ARI) (see **Methods** for definitions).

792

793

794

795

796

797

798

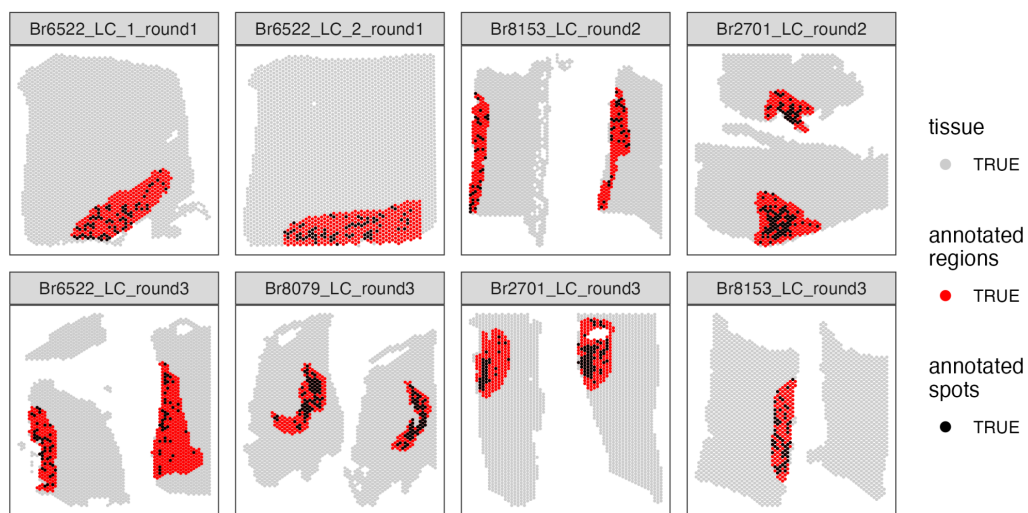
799

800

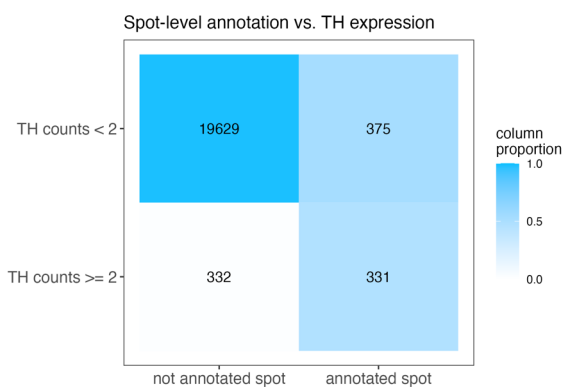
801

802

A Annotations



B



803

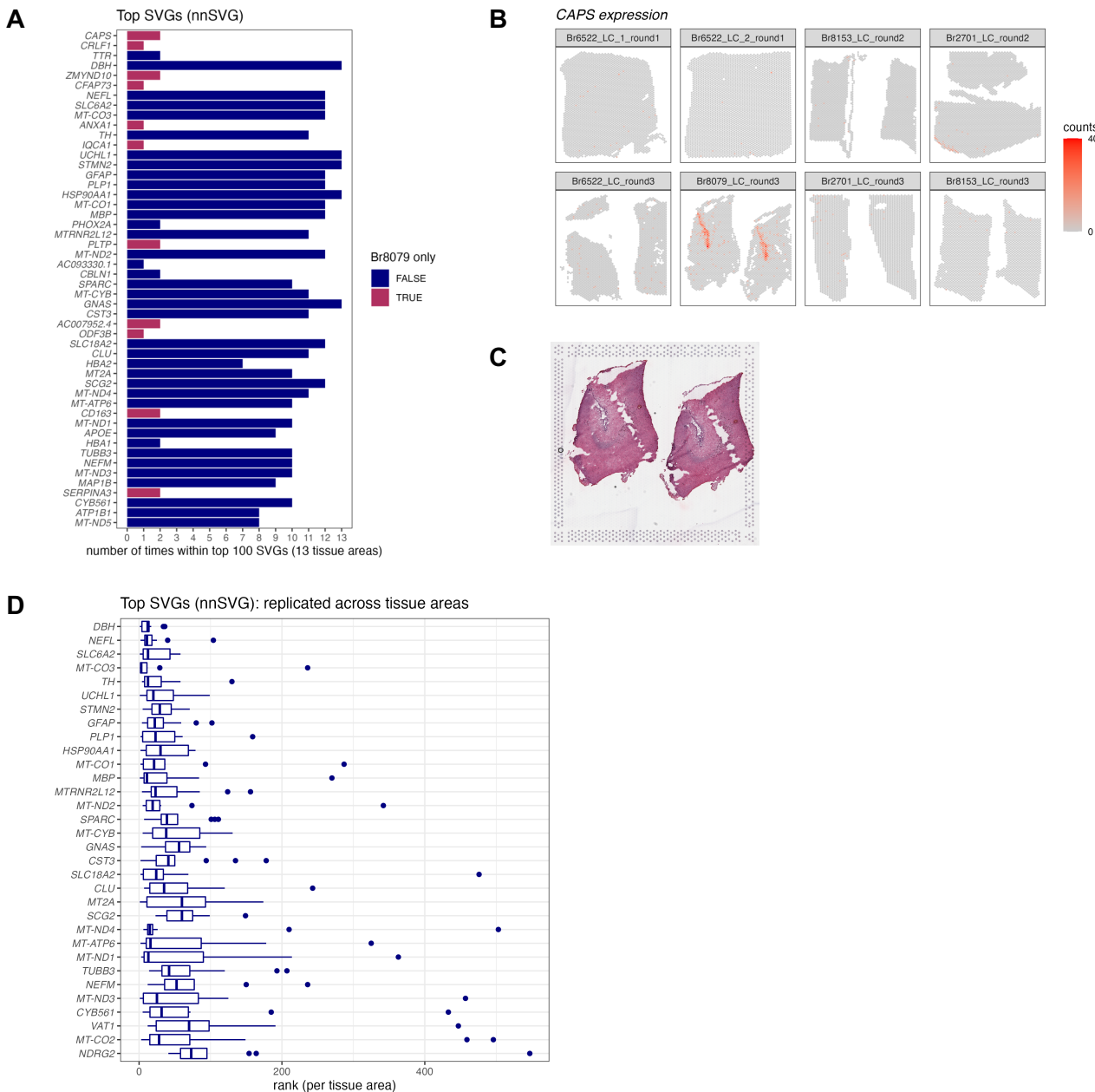
Supplementary Figure 6: Comparison of spot-level and region-level manual annotations in SRT data. (A)

804 We manually annotated individual Visium spots (black) overlapping with NE neuron cell bodies within the
805 previously manually annotated LC regions (red), based on pigmentation, cell size, and morphology from the H&E
806 stained histology images, in the $N=8$ Visium samples. (B) We observed relatively low overlap between spots with
807 expression of the NE neuron marker gene *TH* (≥ 2 observed UMI counts per spot) and the set of annotated
808 individual spots. The differences included both false positives (annotated spots that were not *TH*+) and false
809 negatives (*TH*+ spots that were not annotated). Therefore, we did not use the spot-level annotations for
810 subsequent analyses, and instead used the LC region-level annotations for all further analyses.
811

812

813

826

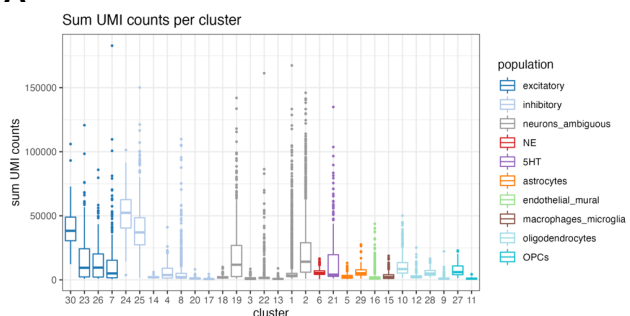


827

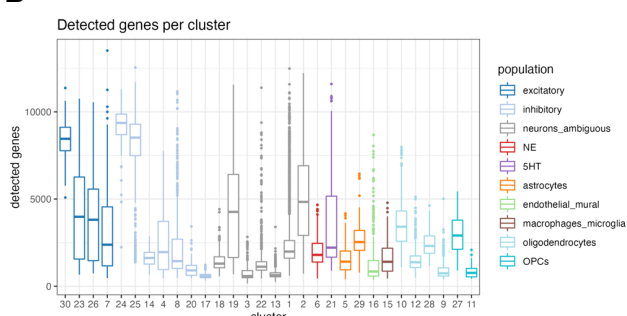
Supplementary Figure 8: Results from applying nnSVG to identify spatially variable genes (SVGs) in SRT data. We applied nnSVG [38], a method to identify spatially variable genes (SVGs), in the Visium SRT samples. We ran nnSVG within each contiguous tissue area containing a manually annotated LC region (13 tissue areas in the $N=8$ Visium samples) and calculated an overall ranking of top SVGs by averaging the ranks per gene from each tissue area. **(A)** The top 50 ranked SVGs from this analysis included a subset (11 out of 50) of genes that were highly ranked in samples from only one donor (Br8079, genes highlighted in maroon). We determined that this was due to the inclusion of a section of the choroid plexus adjacent to the LC for this donor. Bars show the number of times (out of 13 tissue areas) each gene was included within the top 100 SVGs. Rows are ordered by overall average ranking in descending order. **(B)** Spatial expression of CAPS, a choroid plexus marker gene, in the $N=8$ Visium samples. **(C)** Histology image showing the two tissue areas for sample Br8079_LC_round3. **(D)** In order to focus on LC-associated SVGs, we calculated an overall average ranking of SVGs that were each included within the top 100 SVGs in at least 10 out of the 13 tissue areas, which identified 32 highly-ranked, replicated LC-associated SVGs. Boxplots show the ranks in each tissue area. Rows are ordered by the overall average ranking in descending order.

841

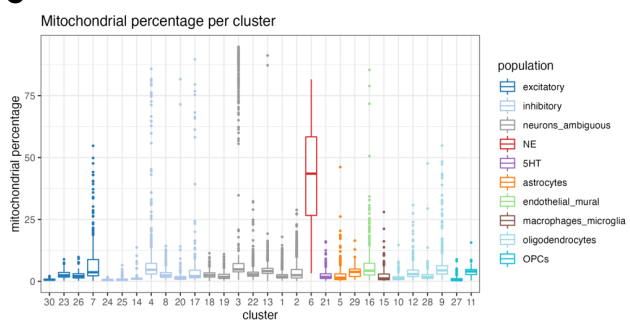
A



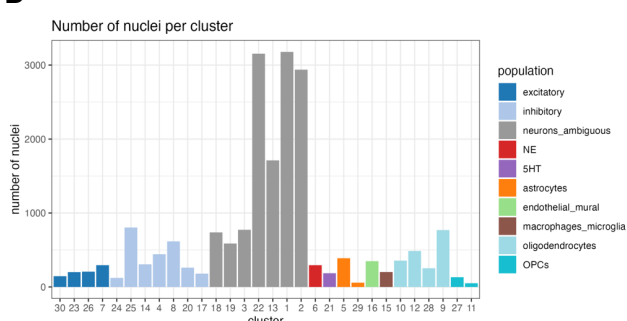
B



C



D



842

843

Supplementary Figure 9: Distribution of nucleus-level quality control (QC) metrics across unsupervised clusters in snRNA-seq data. (A) Sum of UMI counts per nucleus and cluster, **(B)** total number of detected genes per nucleus and cluster, **(C)** percentage of mitochondrial reads per nucleus and cluster, and **(D)** number of nuclei per cluster. We observed an unexpectedly high percentage of mitochondrial reads in the NE neuron cluster (cluster 6, red, C). Since NE neurons were of particular interest for analysis, we did not remove nuclei with a high percentage of mitochondrial reads during QC filtering.

844

845

846

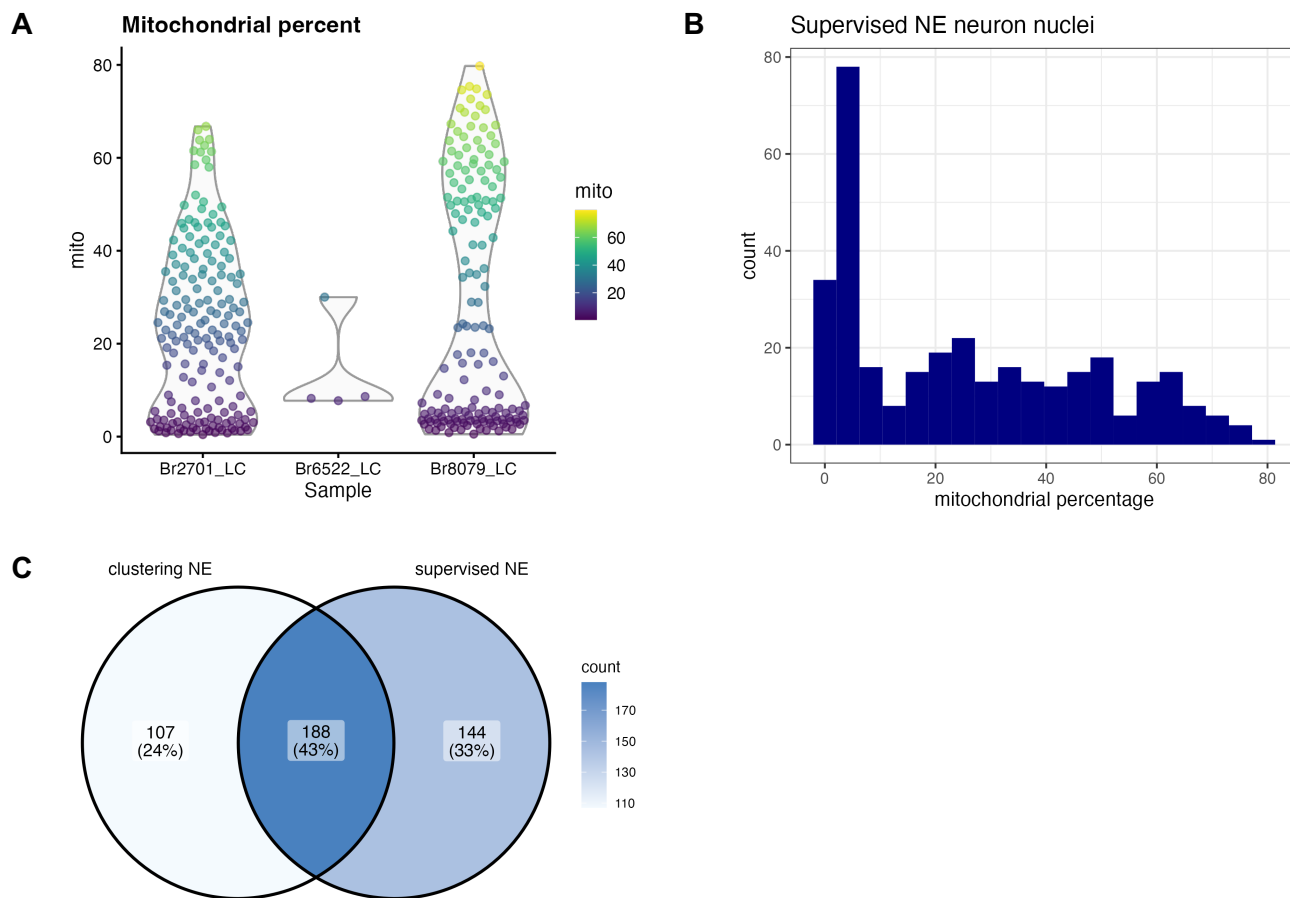
847

848

849

850

851



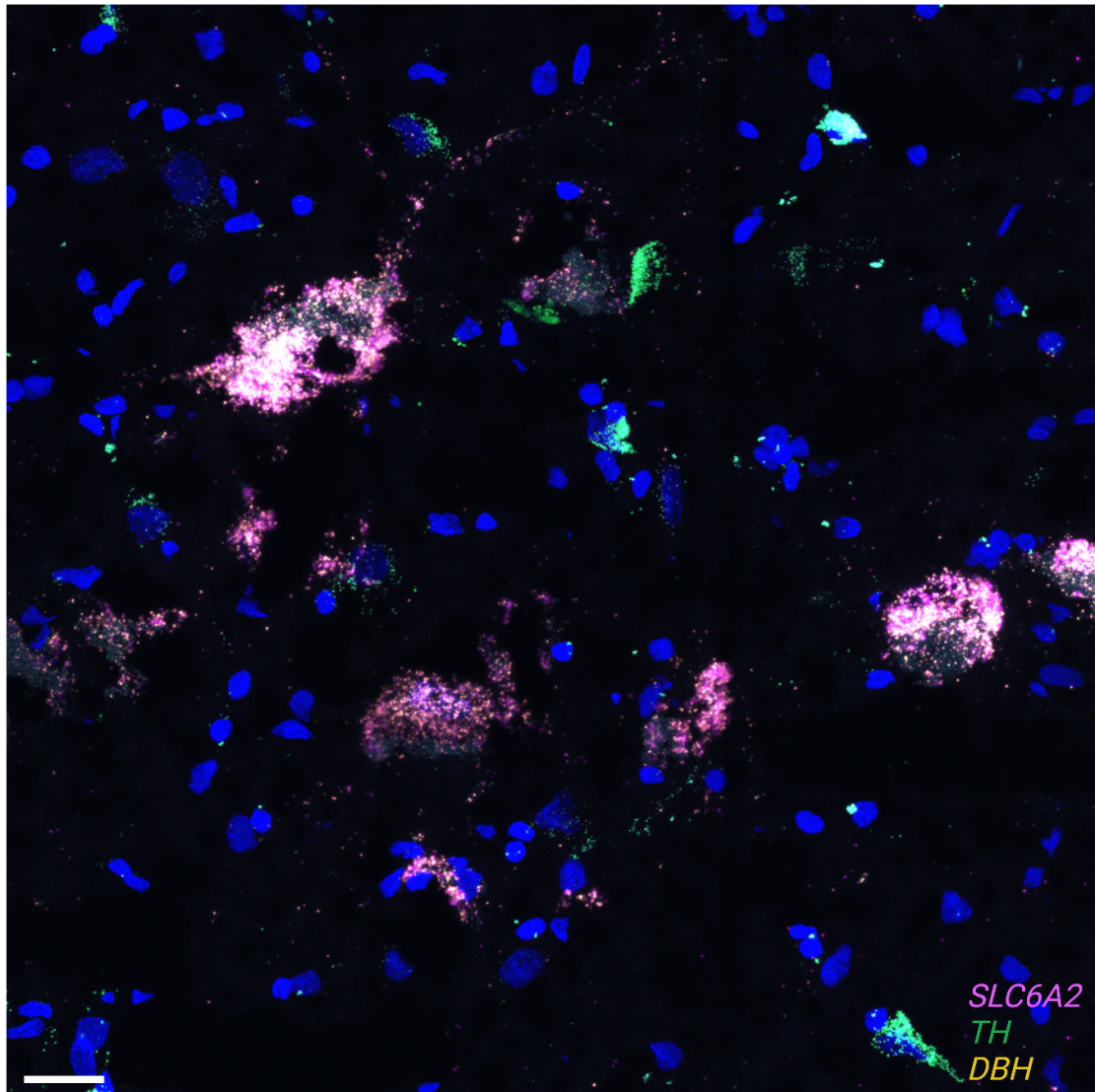
852

853 **Supplementary Figure 10: Supervised identification of NE neuron nuclei by thresholding on expression of**
854 **NE neuron marker genes in snRNA-seq data.** We applied a supervised strategy to identify NE neuron nuclei by
855 simply thresholding on expression of NE neuron marker genes (selecting nuclei with ≥ 1 UMI counts of both *DBH*
856 and *TH*). We observed a higher than expected proportion of mitochondrial reads within this set of nuclei, and did
857 not filter on this parameter during QC processing, in order to retain these nuclei. **(A)** Percentage of mitochondrial
858 reads within the supervised set of nuclei by donor (Br2701, Br6522, and Br8079). **(B)** Histogram showing
859 percentage of mitochondrial reads within the supervised set of nuclei across all donors. **(C)** Venn diagram
860 showing overlap between NE neuron cluster identified by unsupervised clustering (left) and NE neuron population
861 identified by supervised thresholding (right). Values display number of nuclei.

862

863

864



865

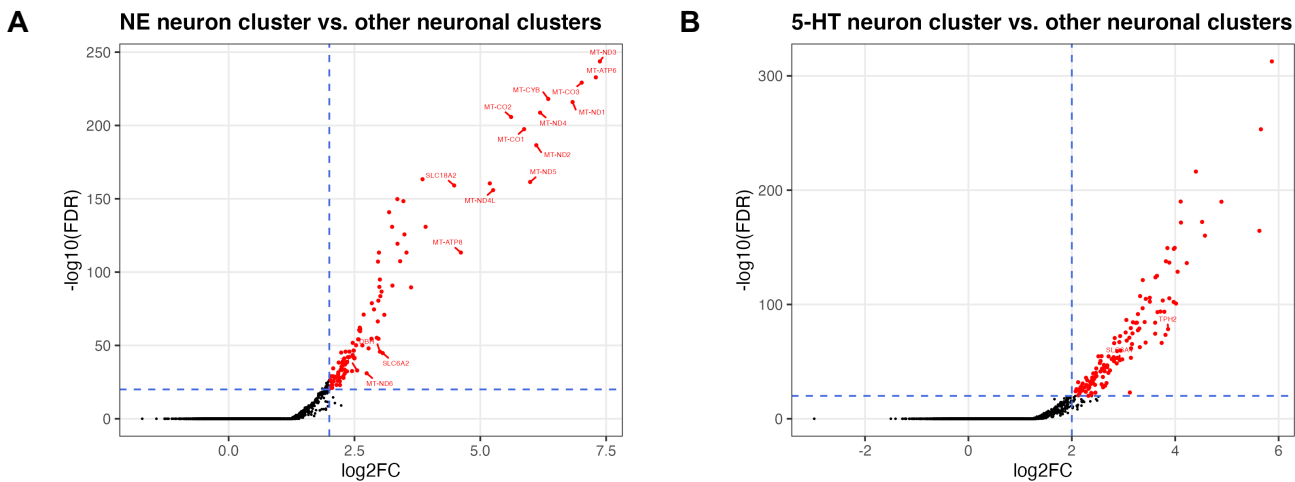
866

867 **Supplementary Figure 11: Expression of NE neuron marker genes in individual cells using RNAscope and**
868 **high-magnification confocal imaging.** We applied RNAscope [32] and high-magnification confocal imaging to
869 visualize expression of NE neuron marker genes (*DBH* in yellow, *TH* in green, and *SLC6A2* in pink, with white
870 representing all three colors overlapping) and DAPI stain for nuclei (blue) on additional tissue sections from an
871 additional independent donor, Br8689. The figure displays a region from a single tissue section, demonstrating
872 clear co-localization of expression of the three NE neuron marker genes (white points) within individual cells.
873 Scale bar: 20 μ m.

874

875

876

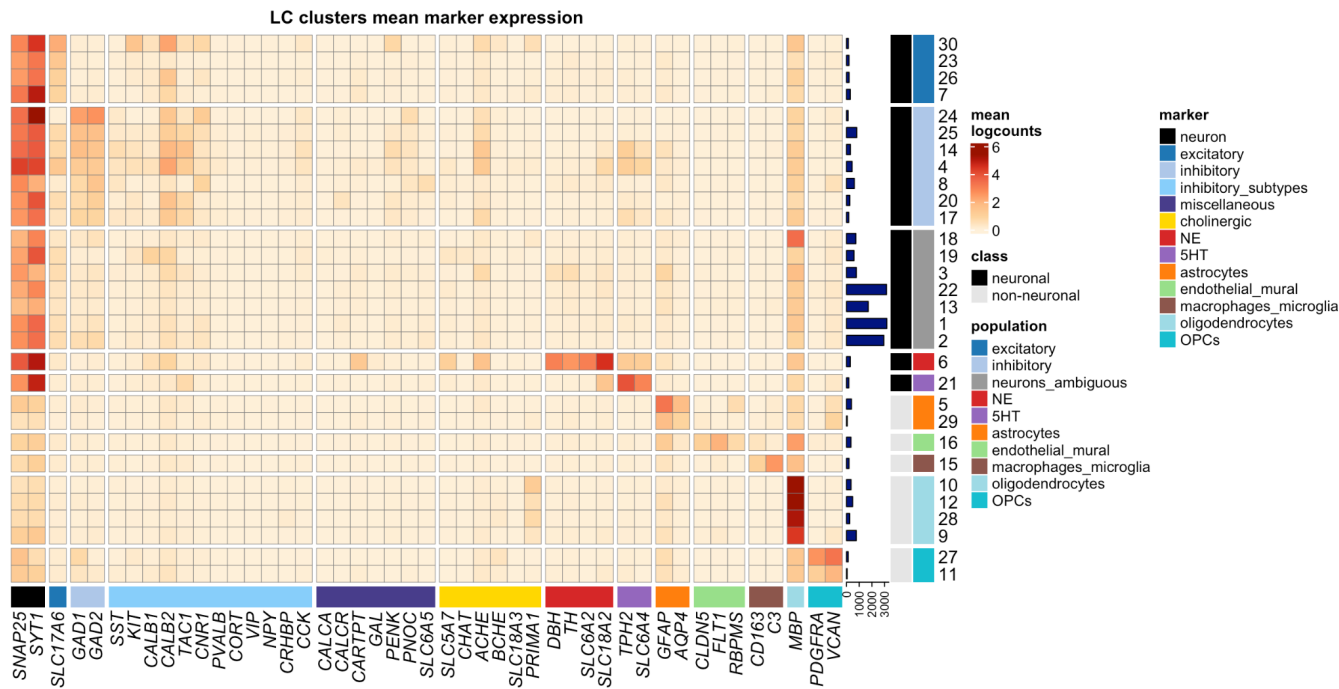


877

878 **Supplementary Figure 12: DE testing results between neuronal clusters in the LC and surrounding region**
879 **in snRNA-seq data. (A)** Volcano plot showing 327 statistically significant DE genes (FDR < 0.05 and FC > 2)
880 elevated in expression within the NE neuron cluster compared to all other neuronal clusters captured in this
881 region. The significant DE genes include known NE neuron marker genes (*DBH*, *TH*, *SLC6A2*, and *SLC18A2*)
882 and mitochondrial genes. **(B)** Volcano plot showing 361 statistically significant DE genes (FDR < 0.05 and FC > 2)
883 elevated in expression within the 5-HT neuron cluster compared to all other neuronal clusters captured in this
884 region. The significant DE genes include known 5-HT neuron marker genes (*TPH2* and *SLC6A4*). Vertical axes
885 are on reversed \log_{10} scale, and horizontal axes are on \log_2 scale. Additional details are provided in
886 **Supplementary Tables 4, 5.**

887
888

889



890
891

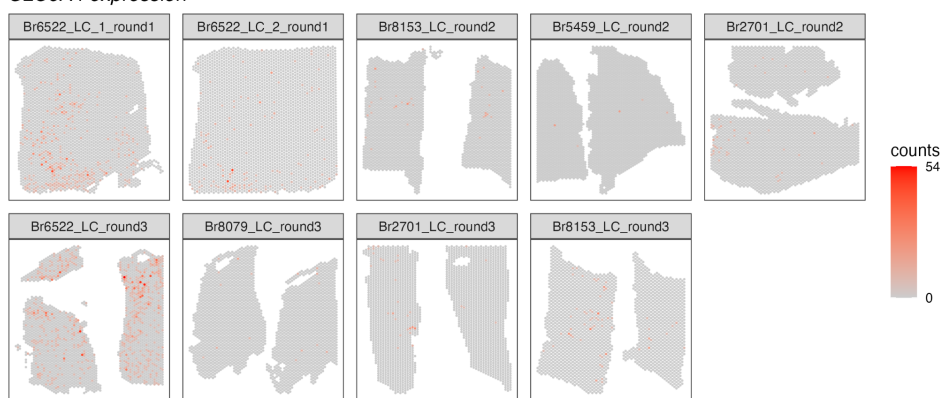
892 **Supplementary Figure 13: Unsupervised clustering results showing additional inhibitory neuronal,
893 miscellaneous, and cholinergic marker genes in snRNA-seq data.** Extended form of heatmap displayed in
894 **Figure 3A**, showing additional inhibitory neuronal marker genes (light blue), miscellaneous marker genes
895 including neuropeptides and receptors included for comparison with [27] (dark blue-purple), and cholinergic
896 marker genes (yellow). We observed diversity in expression of inhibitory neuronal marker genes across inhibitory
897 neuronal subpopulations (additional results in **Supplementary Figure 16**), and we observed expression of
898 cholinergic marker genes within NE neurons (additional results in **Supplementary Figure 18**).
899
900

901

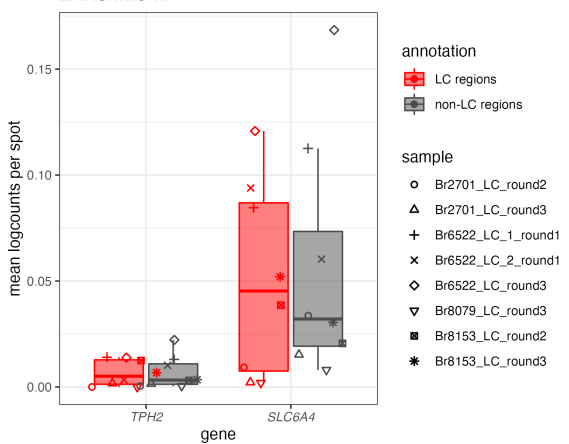
A TPH2 expression



B SLC6A4 expression



C Enrichment



902

903

Supplementary Figure 14: Spatial expression and enrichment analysis of 5-HT neuron marker genes in Visium SRT samples. (A-B) We visualized the spatial expression of 5-HT (5-hydroxytryptamine or serotonin) neuron marker genes (*TPH2* and *SLC6A4*) in the $N=9$ initial Visium SRT samples within the Visium SRT samples, which showed that the population of 5-HT neurons was distributed across both the LC and non-LC regions. **(C)** Enrichment of 5-HT neuron marker gene expression (*TPH2* and *SLC6A4*) within manually annotated LC regions compared to non-LC regions in the $N=8$ Visium SRT samples. Boxplots show values as mean log-transformed normalized counts (logcounts) per spot within each region per sample, with samples represented by shapes.

904

905

906

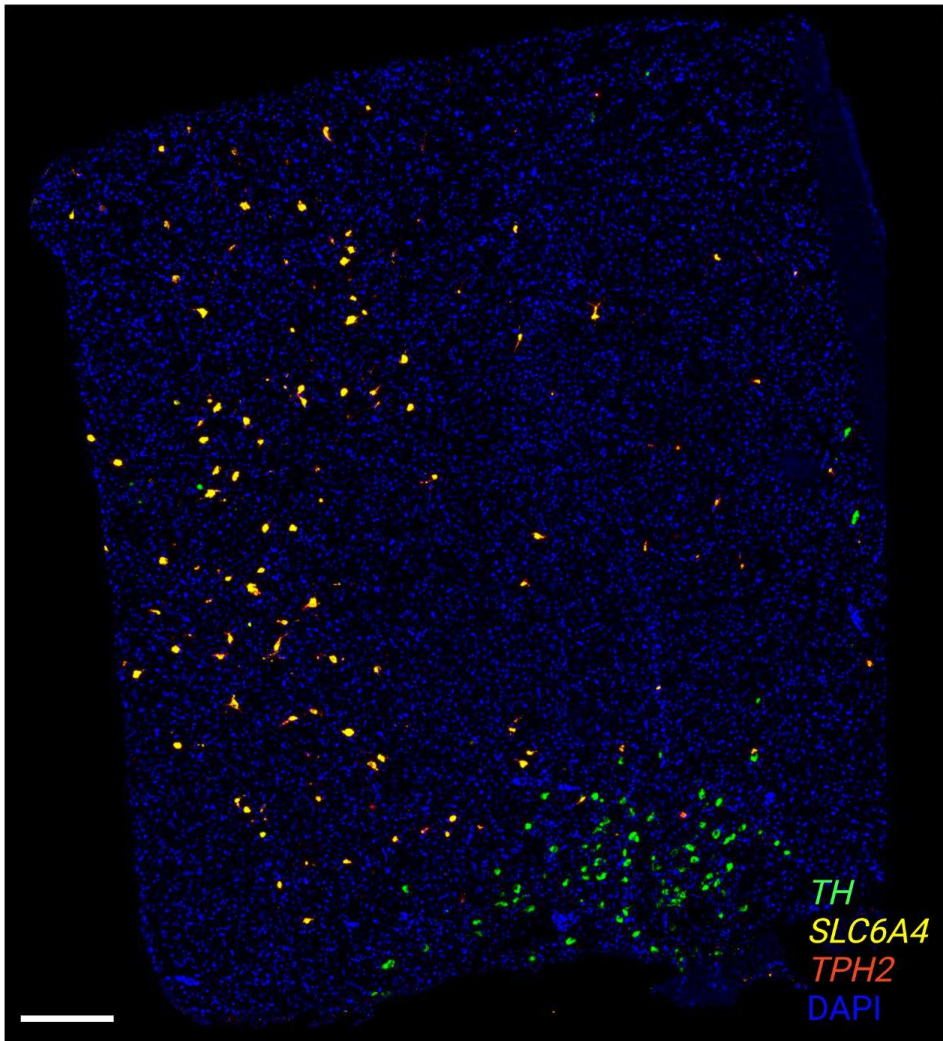
907

908

909

910

911



912

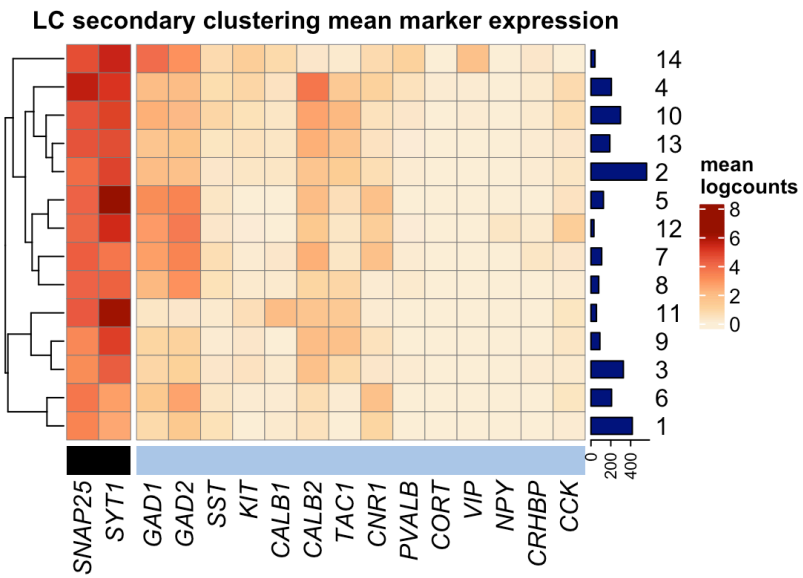
913

914 **Supplementary Figure 15: Expression of NE neuron and 5-HT neuron marker genes using RNAscope.** We
915 applied RNAscope [32] to visualize expression of an NE neuron marker gene (*TH*) as well as 5-HT neuron marker
916 genes (*TPH2* and *SLC6A4*) within an additional tissue section from donor Br6522, demonstrating that the NE and
917 5-HT marker genes were expressed within distinct cells and that the NE and 5-HT neuron populations were not
918 localized within the same regions. Scale bar: 500 μ m.

919

920

921



922

923

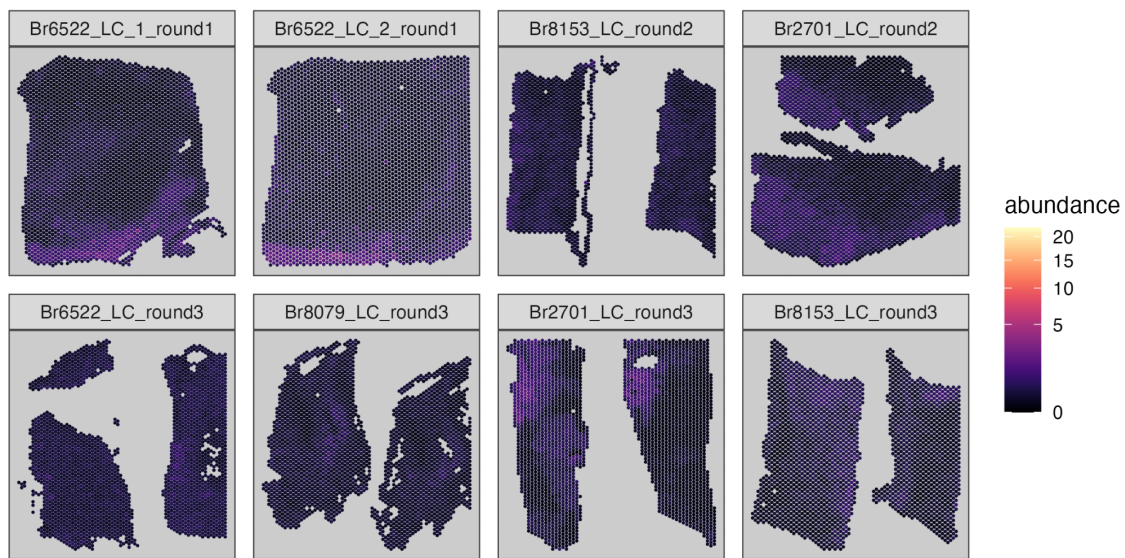
924 **Supplementary Figure 16: Inhibitory neuronal subpopulations identified by secondary unsupervised**
925 **clustering on inhibitory neurons in snRNA-seq data.** We applied a secondary round of unsupervised
926 clustering to the inhibitory neuron nuclei identified in the first round of clustering. This identified 14 clusters
927 representing inhibitory neuronal subpopulations. Heatmap displays expression of neuronal marker genes (black)
928 and inhibitory neuron marker genes (light blue) (columns) in the 14 clusters (rows). Cluster IDs are shown in
929 labels on the right, and numbers of nuclei per cluster are shown in horizontal bars on the right. Heatmap values
930 represent mean log-transformed normalized counts (logcounts) per cluster.

931

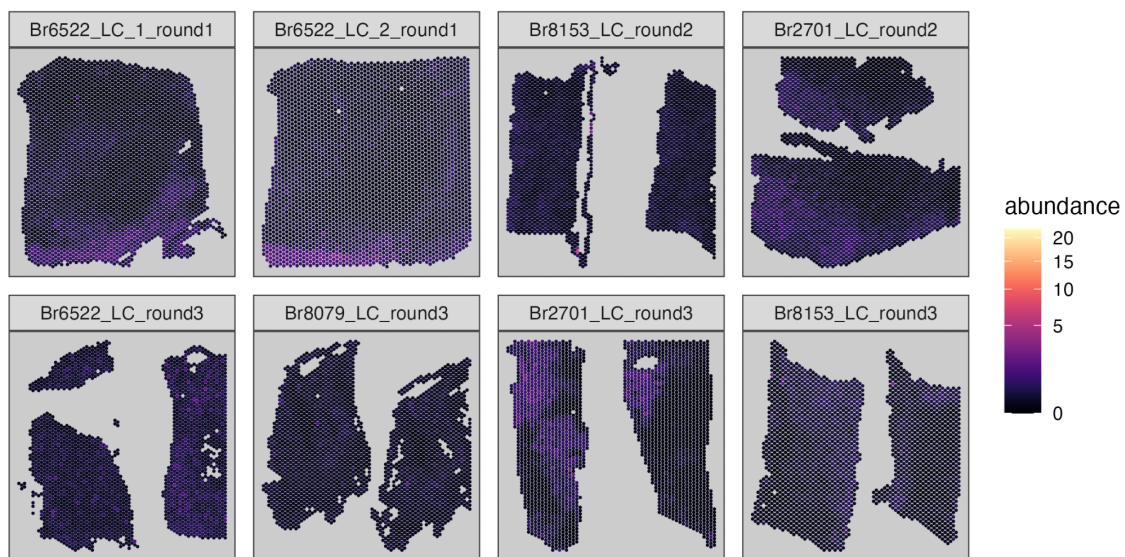
932

933

A Cluster 6



B Cluster 21



934

935

936

937

938

939

940

941

942

943

Supplementary Figure 17: Spot-level deconvolution to map the spatial coordinates of snRNA-seq

populations within the Visium SRT samples. We applied a spot-level deconvolution algorithm (cell2location

[41]) to integrate the snRNA-seq and SRT data by estimating the cell abundance of the snRNA-seq populations,

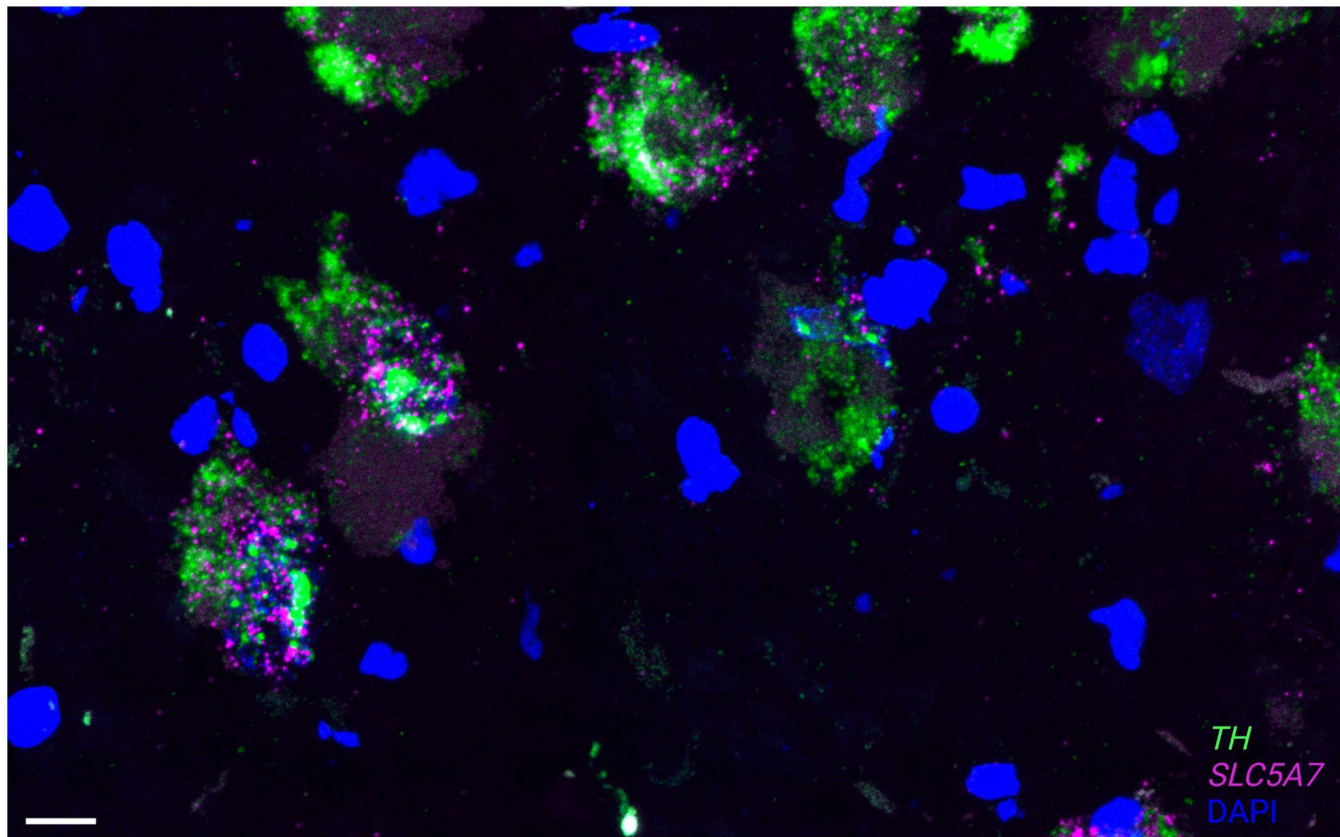
which are used as reference populations, at each spatial location (spot) in the Visium SRT samples. This correctly

mapped **(A)** NE neurons (cluster 6) and **(B)** 5-HT neurons (cluster 21) to the spatial regions where these

populations were previously identified based on expression of marker genes (**Supplementary Figures 2 and 14**).

However, the estimated absolute cell abundance of these populations per spot was higher than expected.

944



945

946

947

948

949

950

951

952

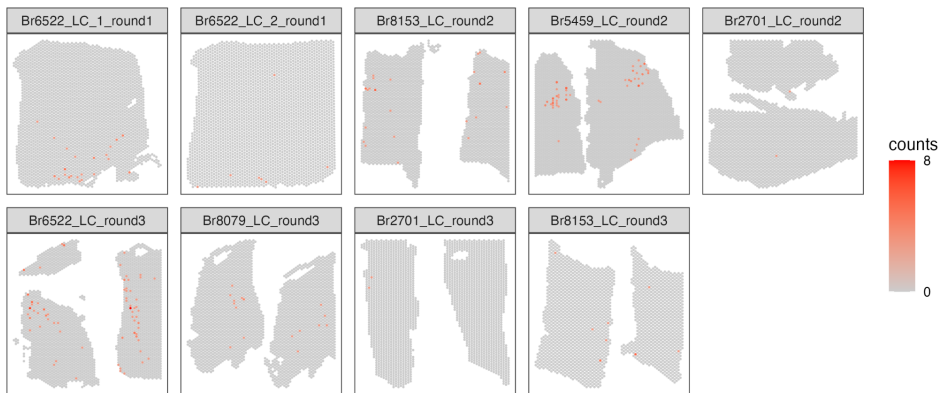
953

954

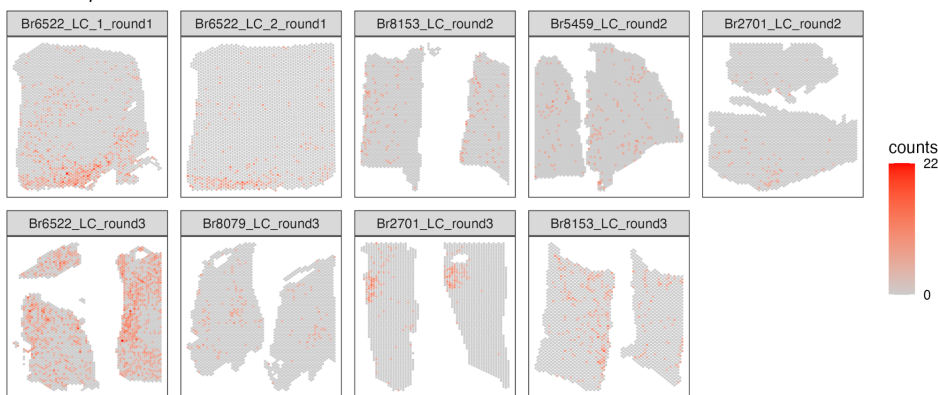
Supplementary Figure 18: High-resolution images demonstrating co-expression of cholinergic marker gene within NE neurons. We applied RNAscope [32] and high-resolution imaging at 63x magnification to visualize expression of *SLC5A7* (cholinergic marker gene encoding the high affinity choline transporter, shown in pink) and *TH* (NE neuron marker gene encoding tyrosine hydroxylase, shown in green), and DAPI stain for nuclei (blue), in a tissue section from donor Br8079. This confirmed co-expression of *SLC5A7* and *TH* within individual cells. Scale bar: 25 μ m.

955

A *SLC5A7* expression



B *ACHE* expression



956

957

Supplementary Figure 19: Spatial expression of cholinergic marker genes in Visium SRT samples.

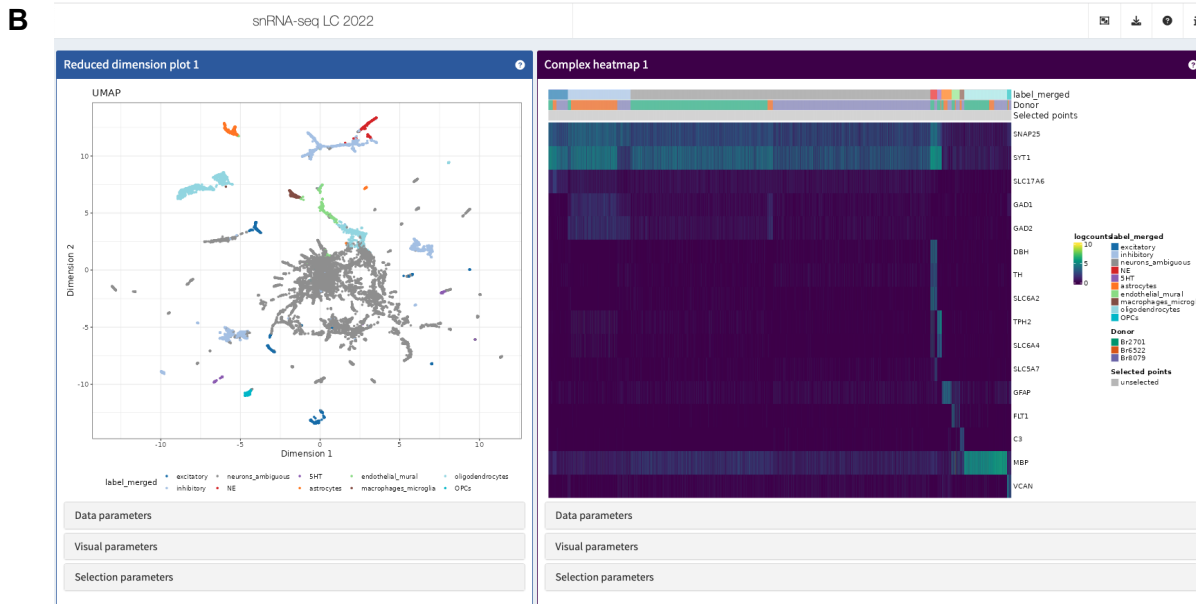
We visualized the spatial expression of cholinergic marker genes **(A)** *SLC5A7* and **(B)** *ACHE* in the $N=9$ initial Visium SRT samples, which showed that these genes were expressed both within and outside the annotated LC regions. Color scale shows UMI counts per spot.

960

961

962

963



964

965 **Supplementary Figure 20: Interactive web-accessible data resources.** All datasets described in this
 966 manuscript are freely accessible via interactive web apps and downloadable R/Bioconductor objects (see **Table 1**
 967 for details). **(A)** Screenshot of Shiny [42] web app providing interactive access to Visium SRT data. **(B)**
 968 Screenshot of iSEE [43] web app providing interactive access to snRNA-seq data.

969

970

971 Back Matter

972 Acknowledgments

973 The authors would like to extend their gratitude to the families and next of kin of the donors for their
974 generosity in supporting and expanding our knowledge of the human brain and neuropsychiatric
975 disease. We would also like to thank the physicians and staff of the Office of the Chief Medical
976 Examiner of the State of Maryland, the Western Michigan University Homer Stryker MD School of
977 Medicine, Department of Pathology, and the Department of Pathology, University of North Dakota
978 School of Medicine and Health Sciences Medical Examiners' office. We would also like to extend our
979 appreciation to Drs. Lewellyn Bigelow and Fernando Goes, and Amy Deep-Soboslay for their provision
980 of the detailed diagnostic evaluation of each case used in this study, James Tooke for his assistance
981 with coordinating dissections within the Lieber Institute for Brain Development (LIBD) Human Brain
982 Repository and Daniel Weinberger for suggestions and advice on the manuscript.

983 Author Contributions

984 Conceptualization: KRM, KM, SCH
985 Data Curation: LMW, HRD, MNT, MT
986 Formal Analysis: LMW, MNT
987 Funding acquisition: LMW, KRM, KM, SCH
988 Investigation: HRD, MNT, SHK, AS, KDM
989 Methodology: HRD, SHK, MNT, KRM
990 Project Administration: KRM, KM, SCH
991 Resources: RB, JEK, TMH
992 Software: LMW, HRD, LCT
993 Supervision: SCP, KRM, KM, SCH
994 Validation: HRD
995 Visualization: LMW, HRD, MT
996 Writing – original draft: LMW, HRD, MNT, KM, SCH
997 Writing – review & editing: LMW, HRD, MNT, KRM, KM, SCH

998 Funding

999 Research reported in this publication was supported by the Lieber Institute for Brain Development,
000 National Institutes of Health awards U01MH122849 (KM, SCH), R01DA053581 (KM, SCH),
001 K99HG012229 (LMW), and awards CZF2019-002443 and CZF2018-183446 (SCH) from the Chan
002 Zuckerberg Initiative DAF, an advised fund of Silicon Valley Community Foundation.

003 Competing Interests

004 The authors declare that they have no competing interests. Matthew N. Tran (MNT) is now a full-time
005 employee at 23andMe and whose current work is unrelated to the contents of this manuscript. His
006 contributions to this manuscript were made while previously employed at the Lieber Institute for Brain
007 Development (LIBD).

008 Code Availability

009 Code scripts to reproduce all analyses and figures in this manuscript, including the computational
010 analysis workflows for the snRNA-seq and SRT data, are available from GitHub at
011 <https://github.com/lmweber/locus-c>. We used R version 4.2 and Bioconductor version 3.15 packages
012 for analyses in R.

013 Data Availability

014 The datasets described in this manuscript are freely accessible in web-based formats from
015 https://libd.shinyapps.io/locus-c_Visium/ (Shiny [42] app containing Visium SRT data) and
016 https://libd.shinyapps.io/locus-c_snRNA-seq/ (iSEE [43] app containing snRNA-seq data), and in
017 R/Bioconductor formats from <https://bioconductor.org/packages/WeberDivechaLCdata> (R/Bioconductor
018 ExperimentHub data package containing Visium SRT data in SpatialExperiment [44] format and
019 snRNA-seq data in SingleCellExperiment [33] format). The R/Bioconductor data package is available in
020 Bioconductor release version 3.16 from Nov 2, 2022 onwards. Instructions to install and access the
021 R/Bioconductor data package are also available from GitHub at
022 <https://github.com/lmweber/WeberDivechaLCdata>. Raw data including FASTQ sequence data files and
023 raw image files will be made available from a Globus endpoint.
024
025

026 References

027 1. Poe GR, Foote S, Eschenko O, Johansen JP, Bouret S, Aston-Jones G, et al. Locus coeruleus: a new look
028 at the blue spot. *Nat Rev Neurosci*. 2020;21: 644–659. doi:10.1038/s41583-020-0360-9

029 2. Chandler DJ, Jensen P, McCall JG, Pickering AE, Schwarz LA, Totah NK. Redefining noradrenergic
030 neuromodulation of behavior: impacts of a modular locus coeruleus architecture. *J Neurosci*. 2019;39:
031 8239–8249. doi:10.1523/JNEUROSCI.1164-19.2019

032 3. Sara SJ. The locus coeruleus and noradrenergic modulation of cognition. *Nat Rev Neurosci*. 2009;10: 211–
033 223. doi:10.1038/nrn2573

034 4. Morris LS, McCall JG, Charney DS, Murrough JW. The role of the locus coeruleus in the generation of
035 pathological anxiety. *Brain Neurosci Adv*. 2020;4: 2398212820930321. doi:10.1177/2398212820930321

036 5. German DC, Walker BS, Manaye K, Smith WK, Woodward DJ, North AJ. The human locus coeruleus:
037 computer reconstruction of cellular distribution. *J Neurosci*. 1988;8: 1776–1788.

038 6. Braak H, Del Tredici K. Neuroanatomy and pathology of sporadic Alzheimer's disease. *Adv Anat Embryol
039 Cell Biol*. 2015;215: 1–162.

040 7. Mravc B, Lejavova K, Cubinkova V. Locus (coeruleus) minoris resistentiae in pathogenesis of Alzheimer's
041 disease. *Curr Alzheimer Res*. 2014;11: 992–1001. doi:10.2174/1567205011666141107130505

042 8. Weinshenker D. Long road to ruin: noradrenergic dysfunction in neurodegenerative disease. *Trends
043 Neurosci*. 2018;41: 211–223. doi:10.1016/j.tins.2018.01.010

044 9. Mather M, Harley CW. The locus coeruleus: essential for maintaining cognitive function and the aging brain.
045 *Trends Cogn Sci (Regul Ed)*. 2016;20: 214–226. doi:10.1016/j.tics.2016.01.001

046 10. Chalermpalanupap T, Weinshenker D, Rorabaugh JM. Down but not out: the consequences of pretangle
047 tau in the locus coeruleus. *Neural Plast*. 2017;2017: 7829507. doi:10.1155/2017/7829507

048 11. Wilson RS, Nag S, Boyle PA, Hizel LP, Yu L, Buchman AS, et al. Neural reserve, neuronal density in the
049 locus ceruleus, and cognitive decline. *Neurology*. 2013;80: 1202–1208.
050 doi:10.1212/WNL.0b013e3182897103

051 12. Grudzien A, Shaw P, Weintraub S, Bigio E, Mash DC, Mesulam MM. Locus coeruleus neurofibrillary
052 degeneration in aging, mild cognitive impairment and early Alzheimer's disease. *Neurobiol Aging*. 2007;28:
053 327–335. doi:10.1016/j.neurobiolaging.2006.02.007

054 13. Andrés-Benito P, Fernández-Dueñas V, Carmona M, Escobar LA, Torrejón-Escribano B, Aso E, et al.
055 Locus coeruleus at asymptomatic early and middle Braak stages of neurofibrillary tangle pathology.
056 *Neuropathol Appl Neurobiol*. 2017;43: 373–392. doi:10.1111/nan.12386

057 14. Braak H, Del Tredici K. Where, when, and in what form does sporadic Alzheimer's disease begin? *Curr
058 Opin Neurol*. 2012;25: 708–714. doi:10.1097/WCO.0b013e32835a3432

059 15. Del Tredici K, Braak H. Dysfunction of the locus coeruleus-norepinephrine system and related circuitry in
060 Parkinson's disease-related dementia. *J Neurol Neurosurg Psychiatr*. 2013;84: 774–783. doi:10.1136/jnnp-
061 2011-301817

062 16. Asherson P, Buitelaar J, Faraone SV, Rohde LA. Adult attention-deficit hyperactivity disorder: key
063 conceptual issues. *Lancet Psychiatry*. 2016;3: 568–578. doi:10.1016/S2215-0366(16)30032-3

064 17. Biederman J, Spencer T. Attention-deficit/hyperactivity disorder (ADHD) as a noradrenergic disorder. *Biol
065 Psychiatry*. 1999;46: 1234–1242. doi:10.1016/s0006-3223(99)00192-4

066 18. Bouret S, Sara SJ. Reward expectation, orientation of attention and locus coeruleus-medial frontal cortex
067 interplay during learning. *Eur J Neurosci*. 2004;20: 791–802. doi:10.1111/j.1460-9568.2004.03526.x

068 19. Bymaster FP, Katner JS, Nelson DL, Hemrick-Luecke SK, Threlkeld PG, Heiligenstein JH, et al.

069 Atomoxetine increases extracellular levels of norepinephrine and dopamine in prefrontal cortex of rat: a
070 potential mechanism for efficacy in attention deficit/hyperactivity disorder. *Neuropsychopharmacology*.
071 2002;27: 699–711. doi:10.1016/S0893-133X(02)00346-9

072 20. Newman LA, Darling J, McGaughy J. Atomoxetine reverses attentional deficits produced by noradrenergic
073 deafferentation of medial prefrontal cortex. *Psychopharmacology (Berl)*. 2008;200: 39–50.
074 doi:10.1007/s00213-008-1097-8

075 21. Kamath T, Abdulraouf A, Burris SJ, Langlieb J, Gazestani V, Nadaf NM, et al. Single-cell genomic profiling
076 of human dopamine neurons identifies a population that selectively degenerates in Parkinson's disease. *Nat
077 Neurosci*. 2022;25: 588–595. doi:10.1038/s41593-022-01061-1

078 22. Maynard KR, Collado-Torres L, Weber LM, Uytingco C, Barry BK, Williams SR, et al. Transcriptome-scale
079 spatial gene expression in the human dorsolateral prefrontal cortex. *Nat Neurosci*. 2021;24: 425–436.
080 doi:10.1038/s41593-020-00787-0

081 23. Tran MN, Maynard KR, Spangler A, Huuki LA, Montgomery KD, Sadashivaiah V, et al. Single-nucleus
082 transcriptome analysis reveals cell-type-specific molecular signatures across reward circuitry in the human
083 brain. *Neuron*. 2021;109: 3088–3103.e5. doi:10.1016/j.neuron.2021.09.001

084 24. Okaty BW, Commons KG, Dymecki SM. Embracing diversity in the 5-HT neuronal system. *Nat Rev
085 Neurosci*. 2019;20: 397–424. doi:10.1038/s41583-019-0151-3

086 25. Mulvey B, Bhatti DL, Gyawali S, Lake AM, Kriaucionis S, Ford CP, et al. Molecular and functional sex
087 differences of noradrenergic neurons in the mouse locus coeruleus. *Cell Rep*. 2018;23: 2225–2235.
088 doi:10.1016/j.celrep.2018.04.054

089 26. Grimm J, Mueller A, Hefti F, Rosenthal A. Molecular basis for catecholaminergic neuron diversity. *Proc Natl
090 Acad Sci USA*. 2004;101: 13891–13896. doi:10.1073/pnas.0405340101

091 27. Luskin AT, Li L, Fu X, Barcomb K, Blackburn T, Li EM, et al. A diverse network of pericoerulear neurons
092 control arousal states. *bioRxiv*. 2022.

093 28. 10x Genomics. Visium Spatial Gene Expression. 2022 [cited 28 Jul 2022]. Available:
094 <https://www.10xgenomics.com/products/spatial-gene-expression>

095 29. 10x Genomics. Chromium Single Cell Gene Expression. 2022 [cited 30 Jul 2022]. Available:
096 <https://www.10xgenomics.com/products/single-cell-gene-expression>

097 30. Counts SE, Mufson EJ. Locus Coeruleus. The human nervous system. Elsevier; 2012. pp. 425–438.
098 doi:10.1016/B978-0-12-374236-0.10012-4

099 31. Maynard KR, Tippani M, Takahashi Y, Phan BN, Hyde TM, Jaffe AE, et al. dotdotdot: an automated
100 approach to quantify multiplex single molecule fluorescent *in situ* hybridization (smFISH) images in complex
101 tissues. *Nucleic Acids Res*. 2020. doi:10.1093/nar/gkaa312

102 32. Wang F, Flanagan J, Su N, Wang L-C, Bui S, Nielson A, et al. RNAscope: a novel *in situ* RNA analysis
103 platform for formalin-fixed, paraffin-embedded tissues. *J Mol Diagn*. 2012;14: 22–29.
104 doi:10.1016/j.jmoldx.2011.08.002

105 33. Amezquita RA, Lun ATL, Becht E, Carey VJ, Carpp LN, Geistlinger L, et al. Orchestrating single-cell
106 analysis with Bioconductor. *Nat Methods*. 2020;17: 137–145. doi:10.1038/s41592-019-0654-x

107 34. Lun ATL, McCarthy DJ, Marioni JC. A step-by-step workflow for low-level analysis of single-cell RNA-seq
108 data with Bioconductor. [version 2; peer review: 3 approved, 2 approved with reservations]. *F1000Res*.
109 2016;5: 2122. doi:10.12688/f1000research.9501.2

110 35. Zhao E, Stone MR, Ren X, Guenthoer J, Smythe KS, Pulliam T, et al. Spatial transcriptomics at subspot
111 resolution with BayesSpace. *Nat Biotechnol*. 2021;39: 1375–1384. doi:10.1038/s41587-021-00935-2

112 36. Korsunsky I, Millard N, Fan J, Slowikowski K, Zhang F, Wei K, et al. Fast, sensitive and accurate integration
113 of single-cell data with Harmony. *Nat Methods*. 2019;16: 1289–1296. doi:10.1038/s41592-019-0619-0

114 37. Gao LL, Bien J, Witten D. Selective inference for hierarchical clustering. *J Am Stat Assoc.* 2022; 1–27.
115 doi:10.1080/01621459.2022.2116331

116 38. Weber LM. nnSVG: scalable identification of spatially variable genes using nearest-neighbor Gaussian
117 processes. *bioRxiv.* 2022.

118 39. Germain P-L, Lun A, Garcia Meixide C, Macnair W, Robinson MD. Doublet identification in single-cell
119 sequencing data using scDblFinder. *F1000Res.* 2021;10: 979. doi:10.12688/f1000research.73600.2

120 40. Ren J, Isakova A, Friedmann D, Zeng J, Grutzner SM, Pun A, et al. Single-cell transcriptomes and whole-
121 brain projections of serotonin neurons in the mouse dorsal and median raphe nuclei. *eLife.* 2019;8.
122 doi:10.7554/eLife.49424

123 41. Kleshchevnikov V, Shmatko A, Dann E, Aivazidis A, King HW, Li T, et al. Cell2location maps fine-grained
124 cell types in spatial transcriptomics. *Nat Biotechnol.* 2022;40: 661–671. doi:10.1038/s41587-021-01139-4

125 42. Chang W, Cheng J, Allaire JJ, Xie Y, McPherson J. shiny: Web Application Framework for R. 2019.

126 43. Rue-Albrecht K, Marini F, Soneson C, Lun ATL. iSEE: Interactive SummarizedExperiment Explorer.
127 [version 1; peer review: 3 approved]. *F1000Res.* 2018;7: 741. doi:10.12688/f1000research.14966.1

128 44. Righelli D, Weber LM, Crowell HL, Pardo B, Collado-Torres L, Ghazanfar S, et al. SpatialExperiment:
129 infrastructure for spatially resolved transcriptomics data in R using Bioconductor. *Bioinformatics.* 2022.
130 doi:10.1093/bioinformatics/btac299

131 45. Fan Y, Chen P, Raza MU, Szebeni A, Szebeni K, Ordway GA, et al. Altered expression of phox2
132 transcription factors in the locus coeruleus in major depressive disorder mimicked by chronic stress and
133 corticosterone treatment in vivo and in vitro. *Neuroscience.* 2018;393: 123–137.
134 doi:10.1016/j.neuroscience.2018.09.038

135 46. Ádori C, Glück L, Barde S, Yoshitake T, Kovacs GG, Mulder J, et al. Critical role of somatostatin receptor 2
136 in the vulnerability of the central noradrenergic system: new aspects on Alzheimer's disease. *Acta
137 Neuropathol.* 2015;129: 541–563. doi:10.1007/s00401-015-1394-3

138 47. Pietrowski MJ, Gabr AA, Kozlov S, Blum D, Halle A, Carvalho K. Glial purinergic signaling in
139 neurodegeneration. *Front Neurol.* 2021;12: 654850. doi:10.3389/fneur.2021.654850

140 48. Moore D, Iritani S, Chambers J, Emson P. Immunohistochemical localization of the P2Y1 purinergic
141 receptor in Alzheimer's disease. *Neuroreport.* 2000;11: 3799–3803. doi:10.1097/00001756-200011270-
142 00041

143 49. Cueto-Ureña C, Mocholí E, Escrivá-Fernández J, González-Granero S, Sánchez-Hernández S, Solana-Orts
144 A, et al. Rnd3 expression is necessary to maintain mitochondrial homeostasis but dispensable for
145 autophagy. *Front Cell Dev Biol.* 2022;10: 834561. doi:10.3389/fcell.2022.834561

146 50. Dong H, Sun Q, Zhang Y, Li Y, Yuan F, Mao S, et al. Genetic deletion of Rnd3 suppresses apoptosis
147 through NF-κB signaling in the brain. *Oncol Rep.* 2021;45: 595–605. doi:10.3892/or.2020.7884

148 51. van Hulzen KJE, Scholz CJ, Franke B, Ripke S, Klein M, McQuillin A, et al. Genetic Overlap Between
149 Attention-Deficit/Hyperactivity Disorder and Bipolar Disorder: Evidence From Genome-wide Association
150 Study Meta-analysis. *Biol Psychiatry.* 2017;82: 634–641. doi:10.1016/j.biopsych.2016.08.040

151 52. Nakashima A, Yamaguchi H, Kodani Y, Kaneko YS, Kawata M, Nagasaki H, et al. Identification by nano-
152 LC-MS/MS of NT5DC2 as a protein binding to tyrosine hydroxylase: Down-regulation of NT5DC2 by siRNA
153 increases catecholamine synthesis in PC12D cells. *Biochem Biophys Res Commun.* 2019;516: 1060–1065.
154 doi:10.1016/j.bbrc.2019.06.156

155 53. Caglayan E, Liu Y, Konopka G. Neuronal ambient RNA contamination causes misinterpreted and masked
156 cell types in brain single-nuclei datasets. *Neuron.* 2022. doi:10.1016/j.neuron.2022.09.010

157 54. Iijima K. Chemocytoarchitecture of the rat locus ceruleus. *Histol Histopathol.* 1993;8: 581–591.

158 55. Iijima K. An immunocytochemical study on the GABA-ergic and serotonin-ergic neurons in rat locus

159 ceruleus with special reference to possible existence of the masked indoleamine cells. *Acta Histochem.*
160 1989;87: 43–57. doi:10.1016/S0065-1281(89)80029-7

161 56. de Leeuw CA, Mooij JM, Heskes T, Posthuma D. MAGMA: generalized gene-set analysis of GWAS data.
162 *PLoS Comput Biol.* 2015;11: e1004219. doi:10.1371/journal.pcbi.1004219

163 57. Lipska BK, Deep-Soboslay A, Weickert CS, Hyde TM, Martin CE, Herman MM, et al. Critical factors in gene
164 expression in postmortem human brain: Focus on studies in schizophrenia. *Biol Psychiatry.* 2006;60: 650–
165 658. doi:10.1016/j.biopsych.2006.06.019

166 58. Zandi PP, Jaffe AE, Goes FS, Burke EE, Collado-Torres L, Huuki-Myers L, et al. Amygdala and anterior
167 cingulate transcriptomes from individuals with bipolar disorder reveal downregulated neuroimmune and
168 synaptic pathways. *Nat Neurosci.* 2022;25: 381–389. doi:10.1038/s41593-022-01024-6

169 59. 10x Genomics. Space Ranger. 9 Oct 2022 [cited 9 Oct 2022]. Available:
170 <https://support.10xgenomics.com/spatial-gene-expression/software/pipelines/latest/what-is-space-ranger>

171 60. McCarthy DJ, Campbell KR, Lun ATL, Wills QF. Scater: pre-processing, quality control, normalization and
172 visualization of single-cell RNA-seq data in R. *Bioinformatics.* 2017;33: 1179–1186.
173 doi:10.1093/bioinformatics/btw777

174 61. Ritchie ME, Phipson B, Wu D, Hu Y, Law CW, Shi W, et al. limma powers differential expression analyses
175 for RNA-sequencing and microarray studies. *Nucleic Acids Res.* 2015;43: e47. doi:10.1093/nar/gkv007

176 62. 10x Genomics. Cell Ranger. 2022 [cited 19 Oct 2022]. Available: <https://support.10xgenomics.com/single-cell-gene-expression/software/pipelines/latest/what-is-cell-ranger>

177